Quaternary Research (2024), 1–21
doi:10.1017/qua.2023.79

Research Article

Lateral and temporal constraints on the depositional history of the Bonneville Salt Flats, Utah, USA

Jeremiah A. Bernau[a,b*], Brenda B. Bowen[a], Charles G. Oviatt[c], Donald L. Clark[b] and Isaac A. Hart[d]

[a]Department of Geology & Geophysics, University of Utah, Salt Lake City, Utah 84112, USA; [b]Utah Geological Survey, Salt Lake City, Utah 84116, USA; [c]Emeritus, Department of Geology, Kansas State University, Manhattan, Kansas 66506, USA and [d]Department of Geography, University of Utah, Salt Lake City, Utah 84112, USA

Abstract

The depositional history of the Bonneville Salt Flats, a perennial saline pan in Utah's Bonneville basin, has poor temporal constraints, and the climatic and geomorphic conditions that led to saline pan formation there are poorly understood. We explore the late Pleistocene to Holocene depositional record of Bonneville Salt Flats cores. Our data challenge the assumption that the saline pan formed from the desiccation of Lake Bonneville, the largest late Pleistocene lake in the Great Basin, which covered this area from 30 to 13 cal ka BP. We test two hypotheses: whether climatic transitions from (1) wet to arid or (2) arid to wet led to saline pan deposition. We describe the depositional record with radiocarbon dating, sedimentological structures, mineralogy, diatom, ostracode, and portable X-ray fluorescence spectrometer measurements. Gypsum and carbonate strontium isotope ratio measurements reflect changes in water sources. Three shallow saline lake to desiccation cycles occurred from >45 and >28 cal ka BP. Deflation removed Lake Bonneville sediments between 13 and 8.3 cal ka BP. Gypsum deposition spanned 8.3 to 5.4 cal ka BP, while the oldest halite interval formed from 5.4 to 3.5 cal ka BP during a wetter period. These findings offer valuable insights for sedimentologists, archaeologists, geomorphologists, and land managers.

Keywords: Evaporites, Carbonates, Lacustrine, Deflation, Pleistocene, Lake Bonneville, Geomorphology, Strontium isotopes, Limnology, Paleoclimate

(Received 18 January 2023; accepted 21 December 2023)

INTRODUCTION

Arid closed-basin lacustrine deposits with evaporites are noteworthy paleoclimate records because of their sensitivity to water balance changes (Lowenstein et al., 1999). Heightened water consumption and increased aridity are causing a decrease in the surface areas of saline lakes globally, which in turn leads to an expansion of exposed lake beds that can become harmful dust sources (Wurtsbaugh et al., 2017; National Academies of Sciences, Engineering and Medicine, 2020). Here, we examine the depositional record of the Bonneville Salt Flats, Utah, USA (BSF), a saline pan within the Great Salt Lake Desert (GSLD) portion of the Bonneville basin (Fig. 1) (Oviatt, 2015; Oviatt and Shroder, 2016). BSF is valued for potash production and recreation, including vehicular land-speed racing (Bowen et al., 2018a). Researchers have extensively studied the hydrology and salt crust dynamics of BSF over the past century (e.g., Nolan, 1927; Turk, 1973; Lines, 1979; Mason and Kipp, 1998; Bowen et al., 2017, 2018b; Bernau and Bowen, 2021). However, BSF's depositional history has poor temporal constraints, and the conditions that led to saline pan formation at BSF are poorly understood. Examination of BSF sediments creates opportunities to explore spatial heterogeneity of depositional dynamics within the Bonneville basin. This investigation is a valuable reference for other underfilled basins, where water and sediment do not fully occupy accommodation space and water loss occurs primarily through evaporation. Moreover, it allows us to gain insights into historical deflation rates and the potential for future dust generation.

We collected and examined BSF cores to determine the depositional history and age of the saline sediments and to test hypotheses about environmental processes leading to saline pan development and alteration. Hypothesis 1 is that the saline pan formed when climate shifted from cool and wet to hot and dry. Hypothesis 2 is that the salt crust at BSF formed when climate shifted from warm and highly arid to cool and wet. Hypothesis 1 tests a long-held presumption that BSF formed from the desiccation of late Pleistocene Lake Bonneville and the evaporative concentration of its fluids (Nolan, 1927; Eardley, 1962; Bowen et al., 2018a). For hypothesis 2 to be true, there must have been an arid period following Lake Bonneville. This arid period would be evidenced by a depositional hiatus, deflation, or records of post–Lake Bonneville arid sedimentation followed by evaporite deposition as the climate changed from arid to wet. We extend our results by coupling BSF's depositional record with Great Basin paleoenvironmental records to delineate temporal changes in deposition and water sourcing in relation to climate change.

***Corresponding author:** Jeremiah A. Bernau; Email: jeremiahbernau@gmail.com

Cite this article: Bernau JA, Bowen BB, Oviatt CG, Clark DL, Hart IA (2024). Lateral and temporal constraints on the depositional history of the Bonneville Salt Flats, Utah, USA. *Quaternary Research* 1–21. https://doi.org/10.1017/qua.2023.79

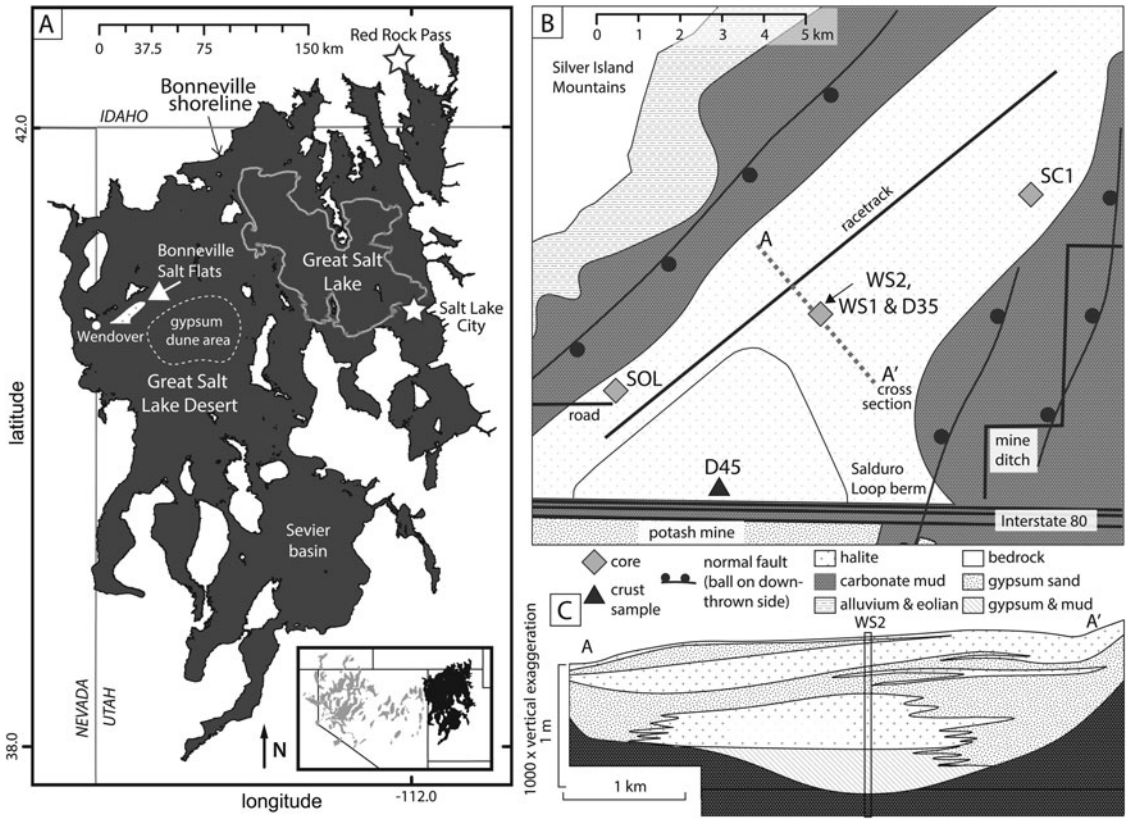

Figure 1. Location overview. (**A**) The location of the Bonneville Salt Flats (BSF) (and general area of sampled gypsum dunes east of the salt flats) relative to the extent of Lake Bonneville. Inset shows location and other late Pleistocene lakes (adapted from Chen and Maloof, 2017). (**B**) BSF salt crust and approximate locations of adjacent Wendover graben normal faults (Clark et al., 2020). Location of primary sediment cores examined in this study shown with squares (WS1 and WS2 are colocated), D45 consists of a surficial halite layer sample. (**C**) Cross section A–A′ of saline pan sediments. (**B and C**) Adapted from Bernau and Bowen (2021).

BACKGROUND

Regional depositional record

Lake Bonneville and Great Salt Lake's (GSL) geologic history and stratigraphy (Fig. 2) form the backdrop for our research. Scientific work on Lake Bonneville began with G. K. Gilbert (1890), has been pursued for generations (e.g., Antevs, 1948; Eardley et al., 1957; Morrison, 1966; Forester, 1987; Thompson et al., 1990; Oviatt et al., 2015; Adams and Bills, 2016; Oviatt and Shroder, 2016), and continues today. Here, we discuss events relative to Lake Bonneville as pre-Bonneville (before ~30 cal ka BP) and post-Bonneville (after 13 cal ka BP). Researchers recently described and interpreted several shallow cores and trenches in GSLD using similar pre- and post-Bonneville terminology (Oviatt et al., 2020; Bernau et al., 2023).

Pre-Bonneville shallow lakes at the location of GSL (Thompson et al., 2016) likely extended into GSLD. Figure 2 shows the lacustrine history of the Bonneville basin during Marine Oxygen Isotope Stages 1 and 2 and the latter part of Marine Isotope Stage 3 (Lisiecki and Raymo, 2005). Erosion has removed Lake Bonneville deposits from the BSF area.

Lake Bonneville sediment layers have distinct sedimentological characteristics (Fig. 2) and distinct freshwater ostracode genera/species assemblages, making them important chronological indicators for interpreting depositional records (Oviatt et al., 1994, 2018; Rey et al., 2016; Oviatt, 2021). Our interpretation of the absence of Bonneville deposits at BSF is confidently ascertained because of the distinctiveness of Bonneville stratigraphy.

Limited evidence exists for post-Bonneville GSLD lakes that would have inundated the BSF area. Ostracode species assemblages indicate GSLD briefly hosted a shallow freshwater lake after 13 cal ka BP. This lake, fed by Sevier basin water, connected with GSL (Palacios-Fest et al., 2021; Fig. 1A). During the Gilbert episode (11.6 cal ka BP), GSL rose to its highest post-Bonneville level at 1295 m (Oviatt, 2014), flooding the BSF area. Researchers have limited knowledge about the history of other post-Bonneville GSL expansions into GSLD and have not identified any shorelines from these expansions (Oviatt et al., 2021). Sediment deposition was minimal due to the brief nature of these expansions.

Bonneville Salt Flats

BSF is located on the western side of the GSLD subbasin of the Bonneville basin (Fig. 1A) on traditionally Newe/Western Shoshone and Goshute lands managed by the U.S. Bureau of Land Management. GSLD is a discharge area for a substantial surrounding watershed (Heilweil and Brooks, 2011) and BSF is the drainage terminus of GSLD's southern portion. Groundwater flow into BSF is important in understanding the saline pan and has been studied over time (e.g., Lines, 1979; Mason and Kipp, 1998). Similarly, aerial images of seasonal ponds and channels to the south and east of BSF indicate that precipitation-sourced overland water flow contributes water to BSF.

The northeast-southwest-trending Wendover graben bounds BSF (Cook et al., 1964; Smith et al., 2012; Clark et al., 2020;

https://doi.org/10.1017/qua.2023.79 Published online by Cambridge University Press

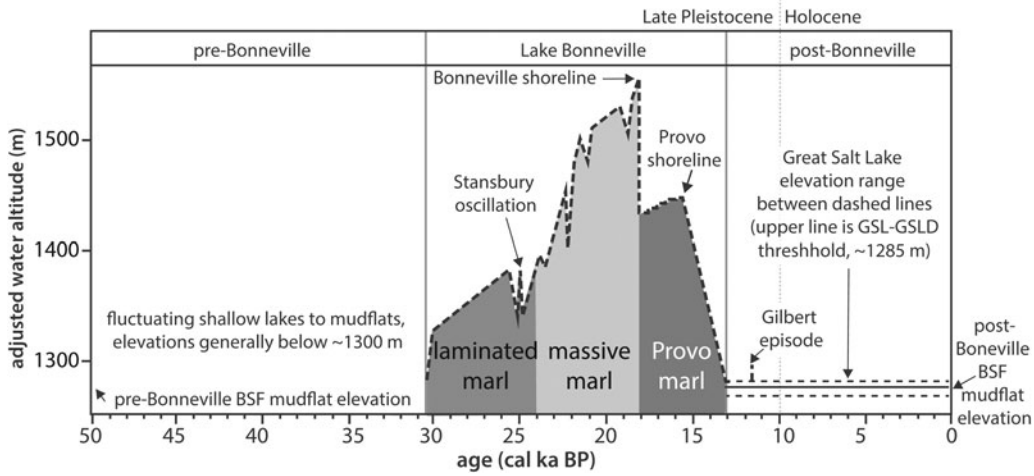

Figure 2. Diagram showing the lacustrine geologic history of the Bonneville basin for the past 30 cal ka BP. Water elevations before 30 cal ka BP are poorly understood. Lake Bonneville deposited a laminated marl as it rose from 30 to 24 cal ka BP. A massive marl was deposited as Lake Bonneville approached its maximum depth (>300 m deep), culminating at the Bonneville shoreline, a distinct bench encircling the basin. At 18 cal ka BP, Lake Bonneville rapidly decreased in level with the Bonneville flood through Red Rock pass to the north (Fig. 1A), stabilizing at the Provo shoreline at 15 cal ka BP and then falling until 13 cal ka BP; the Provo marl was deposited during this period. Elevations are adjusted for differential isostatic rebound in the basin (Oviatt, 2015). Data from Arnow and Stephens (1990), Oviatt (2015), and Oviatt et al. (2021). Elevations of Great Salt Lake (GSL) and Great Salt Lake Desert (GSLD) thresholds from U.S. Geological Survey 7.5 minute quadrangles. BSF, the Bonneville Salt Flats.

Bernau et al., 2023; Fig. 1B). The graben developed during Miocene tectonics (e.g., Miller et al., 2021). BSF is neighbored by a lacustrine mudflat to the east (also referred to as a playa here), the Silver Island Mountains' playa margin and piedmont deposits to the west/northwest, and a potash mine and major interstate highway to the south.

BSF's salt crust overlies layered carbonate mud from a saline lake (Eardley, 1962; Turk et al., 1973; Bowen et al., 2018b). BSF's evaporite sediments consist of a lens-shaped deposit of gypsum and halite with a maximum thickness of ~1.5 m (Bowen et al., 2018b; Fig. 1B and C). Near its center, the base of BSF's evaporites consists of gypsum sand intermixed with carbonate mud (this interval has limited spatial extent). A layer of altered bedded halite overlies the muddy gypsum layer. Much of the primary halite depositional structures within the altered bedded halite layer are replaced by secondary halite growths (Bernau and Bowen, 2021). The saline pan has two primary halite layers: the deeper altered bedded halite layer, which has a limited lateral extent, and the upper halite layer (surficial to near-surface), which covers much of BSF (Fig. 1C). The crust also has small, discontinuous halite layers. Halite beds pinch out to the saline pan edges, whereas gypsum sand layers are more persistent.

METHODS

Four primary sediment cores (SOL, SC1, and colocated cores WS1 and WS2; Table 1) were collected from BSF with a "vibracore" system (Lanesky et al., 1979) in 2017 and 2019 (Table 1). Samples from core D35 (described in Bowen et al., 2018b) and from crust sample D45 (Bernau and Bowen, 2021) were also studied (Fig. 1B). Core sites are located on a northeast-to-southwest transect (Fig. 1B). WS2 and WS1 are located near BSF's evaporite depocenter, SC1 is located on BSF's northeastern edge, and SOL is on its southwestern edge. We selected locations to identify lateral changes in deposition.

We collected primary cores from the surface (or near-surface where the salt crust impeded coring) to up to 4.34 m depth to observe lateral changes in stratigraphic intervals across cores (Table 1). Results do not correct for sediment compression (28 cm compression/m recovered at the SOL coring site and <9 cm compression/m recovered at other sites). Sample depths are reported relative to the top of each core, which is not equal to the ground surface (Table 1).

Coring equipment and details of core-splitting methods are discussed in Hart et al. (2022), which examined other sediment cores using the same methods and facilities. We held the cores in cold storage at the Records of Environment and Disturbance Laboratory at the University of Utah after collection.

Core descriptions and analyses

The four primary cores used in this study were imaged with a Canon EOS 80D digital SLR camera immediately after opening using methods described in Hart et al. (2022). We aligned and stitched high-resolution core images with Hugin software (http://hugin.sourceforge.net). Images of the SOL core were collected at the Continental Scientific Drilling facility with the Geotek Core Imaging System, which collected images with higher stratigraphic contrast than the Canon camera. The bedding, texture, color, sedimentary structures, coring artifacts, and relative grain size of the four primary cores (Supplementary Data) were described and visualized using the PSICAT program, a tool for logging and visualizing macroscopic features (Reed, 2007). Data analyses were conducted in the R programming environment (R Core Team, 2018).

The mineralogy, microfossils, and geochemistry of the four primary cores were examined (Supplementary Data). Changes in mineralogy and microfossil occurrence inform the interpretation of the depositional environment, water chemistry, and chronology. Cores were subsampled at ≤10 cm intervals to determine the presence or absence of rod-shaped carbonate pellets (interpreted as brine shrimp fecal pellet ooids) and ostracode presence and species through visual inspection under a microscope. We treated sediment samples with warm deionized water and wet-sieved

https://doi.org/10.1017/qua.2023.79 Published online by Cambridge University Press

Table 1. Key locations for cores collected from the Bonneville Salt Flats, Utah, USA.[a]

Core name	Core collection date	Latitude (°N)	Longitude (°W)	Core length (m)	Stratigraphic depth of core start (m)	Depth of core top (m)	Depth of core bottom (m)
SOL	December 18, 2017	40.76316	113.89519	3.20	0.00	0.00	4.08
WS1	September 9, 2019	40.78451	113.82990	0.57	0.20	0.22	0.79
WS2	September 9, 2019	40.78451	113.82990	2.90	0.55	0.75	3.52
SC1	September 9, 2019	40.81252	113.77194	3.90	0.10	0.44	4.34

[a]Cores all collected within 1 m of 1284 m elevation. The depth of the core top and bottom is relative to the ground surface. Latitude/longitude data are WGS84.

them using a modification of Forester's (1988) ostracode preparation methodology. We examined the 106–250 μm grain fraction for ostracodes. We determined mineralogy, ostracode fragment, diatom, and chrysophyte cyst presence with smear slide analysis at ≤10 cm intervals (Supplementary Data). We report relative ostracode, whole, and diatom fragment (whether whole, broken, or partially dissolved) and chrysophyte cyst occurrence individually and in aggregate as a percent of the material in each analyzed smear slide; we used this semi-quantitative measure to identify relative changes in biological occurrence over time. Species-level identification of diatoms is beyond the scope of this work and is not discussed here.

We determined X-ray powder diffraction (XRD) bulk mineralogy of mortar and pestle ground powders of SOL samples (n = 16) measured with a Rigaku Mini Flex diffractometer and analyzed with Jade 7 software. We used figure-of-merit values (the quality of fit of X-ray diffraction peaks with those of a known mineral) to identify mineral occurrence and to report relative abundance (Supplementary Data).

X-ray fluorescence spectrometry

We used a Bruker Tracer III-SD energy-dispersive portable X-ray fluorescence spectrometer (pXRF) to detect relative elemental occurrences in the primary cores (Supplementary Data). The goal of measuring elemental occurrences was to aid in interpreting and correlating depositional units and to identify potential environmental changes recorded by qualitative fluctuations in elemental abundances with depth (e.g., Rothwell and Croudace, 2015). The pXRF was mounted on a Dewitt Systems MCS-800 Mobile Core System. Cores were covered with 1.5-μm-thick Spectromembrane Etnom thin film and measured at 2 mm increments. We took 1 minute measurements using two settings: (1) 15 kV, 10 μA, and helium gas; and (2) 40 kV, 30 μA, and yellow filter (25 μm Ti/300 μm Al) without helium.

We used the Bruker ARTAX program to convert pXRF measurements into normalized photon counts for each element. Rather than reporting calibrated concentration data, ARTAX uses Bayesian deconvolution methods to extract net photon counts for each element after removing interference (Elam et al., 2010). Users identify the elements used for deconvolution in ARTAX. We used ARTAX with a minimal number of interpreted elemental occurrences (excluding elements with poor signal); as such, we do not report some elements. Because of potential matrix effects impacting photon counts, we primarily report element photon count ratios in our results.

Strontium isotopes

We measured the $^{87}Sr/^{86}Sr$ isotope ratios of bulk carbonate (n = 5), ostracode shells (n = 6), and gypsum crystals (n = 6) from BSF cores using a Thermo Scientific Neptune multi-collector inductively coupled plasma mass spectrometer using the SrFast method (Mackey and Fernandez, 2011) at the University of Utah Earth Core Facility. We measured $^{87}Sr/^{86}Sr$ isotope ratios of endogenic carbonates and ostracodes to identify possible water provenance and changes in water sourcing (e.g., Hart et al., 2004). Strontium isotope measurements of gypsum layers were made to constrain possible BSF gypsum sources over time. Gypsum sediments were treated with acetic acid to remove carbonates; gypsum was then dissolved with 2 M HCl (Li and Demopoulos, 2005). We made additional $^{87}Sr/^{86}Sr$ isotope ratio measurements of gypsum from GSLD gypsum dunes to the east of BSF (nine samples from seven sites collected by Boden [2016]; Supplementary Data) to determine whether the gypsum in GSLD dunes shared sourcing with BSF gypsum.

Criteria for depositional environment identification

We used criteria for depositional environment identification to aid analysis and stratigraphic unit identification. These criteria are ordered from least to most saline and deepest to shallowest water depths. Environmental interpretations are built on bedding, grain size, mineralogy, and microfossil observations.

Shallow to deep lake deposits primarily consist of clay to silt-sized endogenic minerals, primarily carbonates. Here, an increase in endogenic carbonate precipitation partially identifies shallower, more saline lakes, whereas an increase in detrital sedimentation suggests deeper, less saline lakes. Evidence of fresh water (salinity <0.5 parts per thousand [ppt]) to brackish water (0.5 to 30 ppt) would indicate Lake Bonneville deposits or deposits formed under similar environmental conditions. Freshwater indicators in Lake Bonneville sediments and similar freshwater deposits include relatively abundant and diverse ostracode occurrences, with several species present (DeDeckker and Forester, 1988; Forester et al., 2005; Rey et al., 2016; Oviatt, 2017), high chrysophyte cyst-to-diatom ratios, and high diatom abundance and diversity (Cumming et al., 1993; Clavero et al., 2000; Potapova, 2011; Bae et al., 2020).

We outline criteria to identify saline lakes at three levels of salinity: low (30–70 ppt), moderate (70–150 ppt), and high (>150 ppt). These salinity thresholds are estimates; however, microfossil evidence in analogs (early Lake Bonneville) and modern GSL supports at least three divisions in salinity. More saline-tolerant species, such as brine shrimp and saline-tolerant diatoms, are deposited as lakes transition from brackish to saline. Brine shrimp can adapt to 25–250 ppt salinity, but their optimal salinity is around 80 ppt because of decreased predators at and above this salinity. Brine shrimp cease reproduction above a salinity threshold (~150 ppt in some species) but remain viable (Vanhaecke et al., 1984; Gajardo and Beardmore, 2012). Diatom diversity and chrysophyte cyst-to-diatom ratios decrease with increased salinity.

https://doi.org/10.1017/qua.2023.79 Published online by Cambridge University Press

The ostracode species *Limnocythere staplini* indicates saline water with low alkalinity (Forester, 1983). *Limnocythere staplini* occurs in lakes with salinities ranging from 0.5 ppt (brackish water) to ~50 ppt (saline water; NANODe website: https://www.personal.kent.edu/~alisonjs/nanode); other reports suggest *L. staplini* can tolerate water with >100 ppt sulfate (Delorme, 1969; Forester, 1986). We use the occurrence of monospecific assemblages of *L. staplini* to identify low-salinity saline lakes, similar to the composition of early Lake Bonneville (Oviatt, 2017).

Ostracode presence ceases and diatom abundance and chrysophyte cyst-to-diatom ratios decrease in moderately saline lake deposits. In addition to an absence of ostracodes, moderate-salinity conditions are suggested by the occurrence of brine shrimp (brine shrimp cysts and fecal pellets as rod-shaped ooids). However, because brine shrimp fecal pellet ooids are easily reworked and are persistent over time, their occurrence is not diagnostic of moderate salinity. Whereas rod-shaped ooids have been confirmed to precipitate around GSL brine shrimp fecal pellets (Eardley, 1938; Paradis, 2019), the origin of similar ooids in GSLD from brine shrimp fecal pellets is unconfirmed. Highly saline lakes are inhospitable to brine shrimp and other non-microbial life and often contain evaporite minerals. Highly saline lakes are identified by an absence of microfossils, including brine shrimp cysts. Under these definitions, the south arm of modern GSL (which lacks ostracodes but supports brine shrimp and is <10 m deep on average) is a moderate-salinity saline lake; in contrast, GSL's north arm (which is inhospitable to brine shrimp and other non-microbial life, is relatively shallow, and often contains evaporite minerals; Jagniecki et al., 2021) is a highly saline lake.

Shoreline deposits are diagnostically sandy, potentially consisting of rod-shaped ooids. Deposition of sand beds over unconformities may occur. Although near-lakeshore sediments are not diagnostically indicative of highly saline environments, their stratigraphic occurrence next to sediments deposited in deeper water (fresh water, brackish water, and low- to moderate-salinity saline lakes) indicates low water levels, potentially under highly saline conditions.

Saline pan sediments are the most saline interpreted depositional environment. Saline pan deposition is identified by evaporite mineral accumulation and preservation (gypsum sand and halite).

Chronology

To date sediments, we collected core samples for targeted radiocarbon and optically stimulated luminescence (OSL) analyses (Supplementary Data and Appendix A) and examined a 1-mm-thick volcanic ash layer found in the SOL core at 204.5 cm depth (Appendix B). The Luminescence Lab at Utah State University used the lab's standard procedures to analyze OSL samples (n = 6). The lack of suitable quartz grains for luminescence likely caused disagreement between OSL dates (Appendix A) and stratigraphic markers and radiocarbon dates; as a result, age–depth models did not use OSL dates. Appendix A further describes OSL data. The volcanic ash layer's composition did not match any known ash beds, so it had limited value in determining depositional timing (Appendix B).

Radiocarbon dating

We collected radiocarbon samples from cores SOL, SC1, WS1, WS2, and surface crust sample D45 (Table 2). We processed total organic carbon (TOC) samples, consisting primarily of detrital pollen from saline pan sediments from WS1, WS2, and D45 (Table 2, samples 1–7), at the Records of Environment and Disturbance Lab at the University of Utah. In addition to saline pan sediment TOC samples, we collected one TOC sample from carbonate mud sediment from the WS2 core (Table 2, sample 9). The Center for Applied Isotopic Studies at the University of Georgia analyzed TOC samples. Researchers have satisfactorily dated TOC from similar bedded halite and gypsum sand beds (Cupper, 2006; Xingqi et al., 2008; Zhang and Liu, 2020). We placed saline pan samples in beakers with deionized water to dissolve halite crystals. After halite dissolution, we decanted and filtered samples through a 130 µm sieve to remove large gypsum crystals. To remove carbonates, we treated samples with 10% HCl until effervescence ceased and then centrifuged, decanted, washed with deionized water, and centrifuged and decanted them again. We then used wet slides to screen samples for pollen abundance.

We performed radiocarbon dating of carbonates from ostracodes and bulk sediment samples on SOL, SC1, and WS2 material (Table 2, samples 8 and 10–20). We collected bulk sediment samples from endogenic carbonate–rich intervals to minimize the effect of potential detrital carbonate grains on sample dating. We used settling to separate the finest grain fraction for analysis; this fraction was dried at room temperature and placed into a glass vial. We used the finest grain fraction to ensure that potential carbonate clumps, such as ooids, were not used for dating because of their potentially reworked origin. The impact of detrital fine-grained carbonate material on sample dates is unknown. We handpicked ostracode samples after sieving. To prevent potential measurement of reworked material, we only measured ostracode valves from intervals that consistently had ostracodes across multiple sample depths and used samples that consisted primarily of intact valves. The National Ocean Sciences Accelerator Mass Spectrometry Facility at Woods Hole Oceanographic Institution hydrolyzed bulk sediment and ostracode radiocarbon samples and measured ^{14}C (Table 2) and $\delta^{13}C$ (Supplementary Data).

Age–depth models

Uncalibrated radiocarbon dates (Table 2) show two broad populations of samples: pre-Bonneville (^{14}C ages of 44–30 ka) with some suspect Lake Bonneville dates (^{14}C ages of 26–22 ka), and post-Bonneville (^{14}C ages <7.5 ka). We used identified stratigraphic units to correlate dated carbonate mud intervals (all pre-Bonneville to suspect Lake Bonneville in age) across cores. The stratigraphic correlations enabled us to construct more robust age–depth models (after the methodology of Hart et al. [2022]) based on radiocarbon dates alone. Post-Bonneville radiocarbon ages only came from the evaporite layers. Individual age–depth models were constructed for the carbonate mud interval from each core and for the evaporite layer at BSF's center (Fig. 3). We calibrated radiocarbon dates with the IntCal20 Northern Hemisphere calibration curve (Reimer et al., 2020) using Bacon 2.5.7 with default priors (Blaauw and Christeny, 2011).

Please interpret radiocarbon ages and age–depth model ages with caution, because several unknowns (that are not included in age–depth models because of insufficient information) may influence ages: (1) potential for reworked carbon contamination, (2) possible atmospheric carbon contamination, and (3) an unknown reservoir effect.

Reworked carbon could have been formed long before it was deposited (e.g., as may happen with charcoal or pollen), leading to radiocarbon ages exceeding depositional ages. In the evaporite

https://doi.org/10.1017/qua.2023.79 Published online by Cambridge University Press

Table 2. Radiocarbon results.[a]

^{14}C no.[b]	Core	Core depth (cm)	Lab no.[c]	^{14}C age (ka)	Age error (1σ) (ka)	Mean age (cal ka BP)	Min. and max. age (cal ka BP)	Type[d]
1	D45[e]	6–10	UGAMS-56742	0.57	0.02	0.5	0.4–0.6	Pollen
2	WS1	53–55	UGAMS-56743	3.36	0.02	3.5	3.4–3.7	Pollen
3	WS1	58–61	UGAMS-56741	3.95	0.025	4.1	3.9–4.3	Pollen
4	WS1	73–78	UGAMS-56744	3.98	0.025	4.5	4.4–4.8	Pollen
5	WS2	31–36	UGAMS-56743	4.32	0.025	4.9	4.8–5.1	Pollen
6	WS2	58–61	UGAMS-56741	5.65	0.03	6.4	6.3–6.6	Pollen
7	WS2	78–82	UGAMS-56744	7.48	0.035	8.2	8.0–8.4	Pollen[f]
8	WS2	87	OS-165141	21.6	0.2	24	23–26	Bulk TIC
9	WS2	93–94	UGAMS-57849	24.06	0.07	28	27–29	Pollen[f]
10	WS2	93.5	OS-165140	26.3	0.35	28	27–29	Bulk TIC
11	WS2	150	OS-161136	30.1	0.5	32	31–34	Bulk TIC
12	WS2	247	OS-161137	32.2	0.68	37	35–38	Ostracodes
13	WS2	263	OS-161138	33	0.76	38	36–39	Ostracodes
14	WS2	285.2	OS-161135	34.4	0.87	39	37–40	Bulk TIC
15	SC1	170	OS-161183	34.2	2.5	39	38–40	Ostracodes
16	SC1	285	OS-161179	42.8	3.9	44	43–46	Ostracodes
17	SC1	385	OS-165136	45.7	4	49	47–52	Bulk TIC
18	SOL	174	OS-165137	38.9	1.7	42	40–44	Ostracodes
19	SOL	240	OS-165138	43.7	3.1	45	44–47	Bulk TIC
20	SOL	310	OS-165139	44	3.2	49	47–51	Bulk TIC

[a]Dates calibrated with the IntCal20 Northern Hemisphere calibration curve (Reimer et al., 2020) using Bacon 2.5.7 age–depth models with default priors (Blaauw and Christeny, 2011). The minimum and maximum age denote the age–depth model's 95% confidence interval; it is important to note that this uncertainty is lower than the individual sample age error for several samples. Samples 8 to 10 exhibit dates suggesting a Lake Bonneville origin; however, as Lake Bonneville sediments were absent, these samples consist of reworked sediment (sample 8) or have modern carbon contamination, making them appear younger than they are (samples 9 and 10). Note that sample 17, interpreted as originating from unit VII, has an older age than sample 20 from the underlying unit VIII. This apparent age inversion may be due to high measurement error in the nearly radiocarbon-dead sample, possibly modern carbon contamination, or potentially incorrect interpretation of stratigraphic units.
[b]^{14}C no. denotes sample numbers in Figs. 3, 4, and 6.
[c]Accession numbers refer to the processing laboratories: the Center for Applied Isotopic Studies (UGAMS) and National Ocean Sciences Accelerator Mass Spectrometry Facility (OS).
[d]TIC, total inorganic carbon.
[e]Sample D45 is from a surface block of halite (see Bernau and Bowen, 2021).
[f]Pollen, not identified in sample, but sample treated for pollen, meaning this sample consists of organic carbon. Unidentified pollen or other organic material (e.g., charcoal) likely dated from those samples.

interval, TOC samples could have moved stratigraphically down section through dissolution pipes in bedded halite layers, leading to radiocarbon ages that are younger than depositional ages. Without additional detailed measurements, we cannot quantify the impact of reworked carbon on depositional age determination.

Modern carbon contamination from the atmosphere may have influenced radiocarbon dates, with the greatest impact of this contamination potentially being felt by older radiocarbon-poor samples dating as pre-Bonneville and suspect Lake Bonneville. Researchers have demonstrated that ostracode shells, which have high surface areas (increasing their potential interaction with air), may be impacted by atmospheric modern carbon contamination (Hajdas et al., 2004; Zimmerman et al., 2012). They used progressive acid leaching of samples to demonstrate that samples were >1500 to >6000 yr older than bulk sample measurements initially suggested. Similar experiments on dense calcite increased ages by 500 to 1000 yr over the bulk age. Our research did not use progressive acid leaching to address potential modern carbonate contamination. However, we did use core samples and bulk carbonate sediments with minimal processing to reduce atmospheric contamination. That being considered, some degree of modern carbon contamination is probable.

The reservoir effect is a concern in dating carbonates precipitated from lake water. The reservoir effect leads samples to yield ages older than depositional timing because the water they precipitated from was radiocarbon depleted (old). Our age–depth models did not use reservoir effect corrections, because a radiocarbon reservoir's presence, magnitude, and persistence in pre-Bonneville sediments is unknown. Our one bulk carbonate and TOC sample pair is insufficient to establish a reservoir effect, because potential reworking of material can lead to samples yielding ages that are not reflective of depositional timing; reducing this uncertainty requires measuring several paired samples (e.g., Hart et al., 2022). We recognize the wide range of uncertainties inherent in dating ostracodes and bulk carbonates due to the reservoir effect and potential modern carbon contamination and that resulting errors in the age–depth models may be on the scale of several thousand years for pre-Bonneville carbonate radiocarbon samples (Hajdas et al., 2004; Zimmerman et al., 2012; Thompson et al., 2016; Bowen et al., 2019). Despite these limitations, chronological

https://doi.org/10.1017/qua.2023.79 Published online by Cambridge University Press

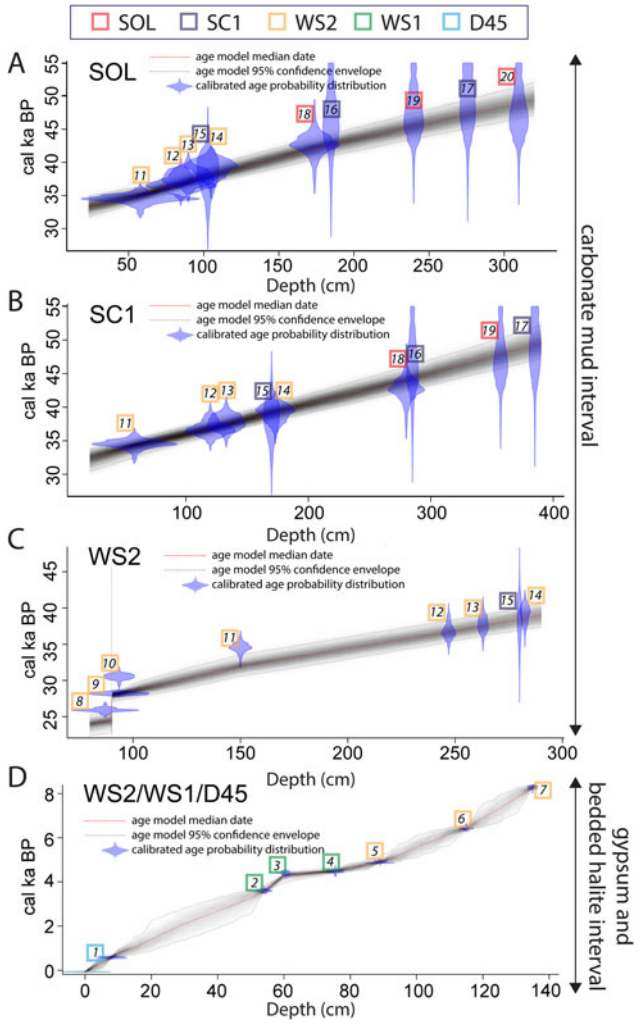

Figure 3. Bacon age–depth models for cores (**A**) SOL, (**B**) SC1, and (**C**) WS2 (which consist primarily of carbonate muds), and (**D**) WS2/WS1/D45 (which consist of gypsum sand and bedded halite; core information in Table 1). This figure illustrates two depositional periods (**A** to **C** and **D**) due to a depositional hiatus between carbonate mud deposition and the subsequent deposition of gypsum and bedded halite. Age–depth models for cores SOL, SC1, and WS2 incorporate dates from the core being presented, along with dates from other cores, with date positions based on stratigraphic matches. (**A to D**) Age–depth models are specific to each core and the investigated interval (saline pan or pre-saline pan); as such, depths are not directly comparable across cores. Blue areas depict the distribution of ^{14}C dates, where a broader *x*-value range indicates higher relative precision. The age–depth model in **D** is derived from multiple cores at the WS site (WS1 and WS2) and a shallow crust sample collected from D45 (Fig. 1B). Refer to Table 2 for additional details on the radiocarbon samples numbered on the figures, with colored boxes around the sample numbers corresponding to the core from which the sample was collected.

results are consistent across cores, exhibiting coherence with depth and adherence to local stratigraphic constraints. This provides a degree of confidence in the presented results.

RESULTS

After providing overarching stratigraphic insights, we offer mineralogical information. We discuss soft-sediment deformation features in Appendix C and outline broad observations from pXRF data in Appendix D. Subsequently, we present strontium isotope measurements, followed by the age–depth models. We use these data sets to identify and describe eight late Pleistocene to Holocene stratigraphic units (ascending from VIII to I) differentiated by microfossil presence and type, mineral composition, and sedimentology (Figs. 4–6).

Broad stratigraphic observations

The WS2, SC1, and SOL cores consist of predominately carbonate-rich sediment with laminated to massive bedding, interspersed with sand-rich intervals. The WS1 core and the uppermost portion of the WS2, SC1, and SOL cores consist of gypsum and halite. We observe several stratigraphic trends. Carbonate-rich, pre–saline pan sediments have three intervals with diatoms and ostracodes and three intervals with little to no diatom or ostracode occurrence (Fig. 4). The ostracode- and diatom-poor intervals have higher proportions of coarse-grained sediment, primarily calcareous rod-shaped ooid-rich sand and clumpy carbonate intervals.

We observe a negative correlation between ostracode occurrence and rod-shaped ooid abundance in all cores. Only monospecific *L. staplini*, used to interpret saline water when in association with other saline indicators, such as brine shrimp cysts or fecal pellets (Oviatt, 2017), are found in BSF core samples, indicating saline depositional periods. Sediments lacking ostracodes indicate moderate- to high-salinity settings inhospitable to ostracodes. No brine shrimp cysts were identified.

The ostracode-rich and ostracode-poor intervals delineated units in the carbonate-rich section. Unit thicknesses, and thus accumulation rates, differ across cores. SC1 and SOL at BSF edges exhibit lower accumulation rates (SOL being the lowest), whereas WS2 near the depocenter shows the highest accumulation rate (Fig. 4).

XRD data

XRD data confirm the mineralogy observed with smear slides (Supplementary Data). Aragonite and halite exist in all samples. We interpret halite occurrence throughout pre–saline pan core sections as a sampling artifact from the desiccation of highly saline pore fluids. Darker-colored core intervals correspond to higher calcite occurrences, whereas aragonite is more abundant in lighter-colored pre–saline pan core intervals. We found gypsum only in saline pan sediments. We also identified quartz, dolomite, ankerite, and Mg-calcite in carbonate mud sediments.

We identified increased proportions of non-aragonite carbonates (dolomite or calcite) in smear slides from nearshore, ooid-rich deposits, indicating a change in brine chemistry near the sites of sand deposition relative to other carbonate depositional environments.

Strontium isotope ratios

Carbonate-rich pre–saline pan sediments exhibit low variation in strontium isotope ratios (mean $^{87}Sr/^{86}Sr$ ratio of 0.7128, standard deviation of 0.0002; Fig. 7B and C; Table 3). Pre–saline pan bulk sediment samples show higher variation than ostracode samples (0.0008 vs. 0.0002 $^{87}Sr/^{86}Sr$ ratio range, respectively), suggesting detrital contamination (Fig. 7C). Saline pan gypsum $^{87}Sr/^{86}Sr$ ratios are within a small range and have lower values (0.7126 $^{87}Sr/^{86}Sr$ ratio) than most pre–saline pan sediment samples (Fig. 7B and C).

https://doi.org/10.1017/qua.2023.79 Published online by Cambridge University Press

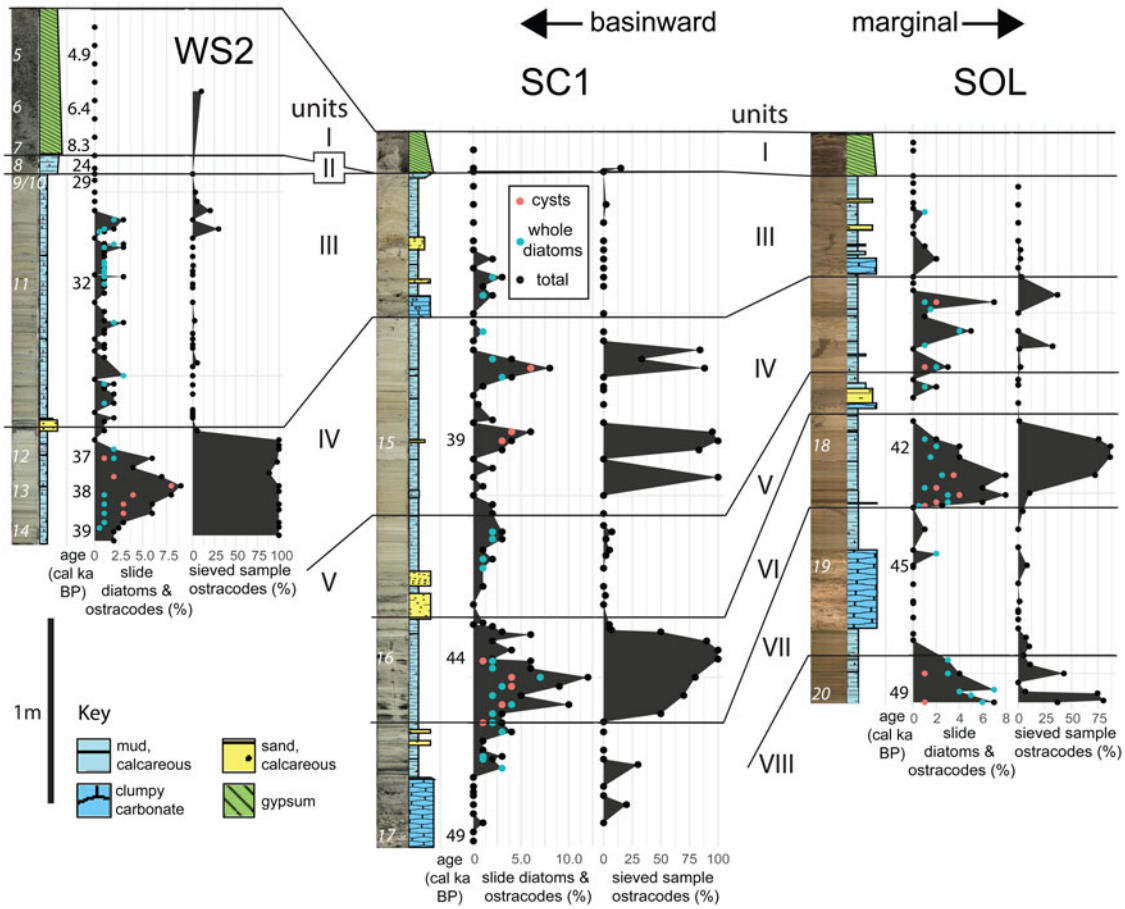

Figure 4. Core data and stratigraphic unit correlation between cores that penetrate the carbonate mud interval. The depocenter, illustrated on the left (WS2), exhibits the thickest units, while the most proximal core (SOL) on the right features the thinnest units. A different imaging technique was employed for SOL (see "Methods"). Radiocarbon sample numbers (white, 5–20) are provided for reference (Table 2). Calcareous sand and clumpy carbonate intervals shown in the lithological column contain abundant rod-shaped ooids. The slide diatoms and ostracode data column uses the semiquantitative estimate of occurrence as percentage of total smear slide material; total occurrence is depicted within the filled area, with chrysophyte cyst and whole diatom percent occurrence noted. The sieved ostracode percent column reports the occurrence of ostracodes in sieved samples (106–250 μm fraction).

$^{87}Sr/^{86}Sr$ ratios of gypsum from GSLD gypsum dunes (Fig. 7A and D; Table 4) are very consistent (mean $^{87}Sr/^{86}Sr$ ratio of 0.7134, standard deviation of 0.0002). Furthermore, there are no spatial trends in dune gypsum $^{87}Sr/^{86}Sr$ ratios. Notably, gypsum dune $^{87}Sr/^{86}Sr$ ratios differ markedly from those in BSF gypsum.

Chronology

Radiocarbon dates reveal two distinct sample populations: pre-Bonneville (^{14}C ages of 44 to 30 ka) with questionable Lake Bonneville dates (^{14}C ages of 26 to 22 ka) and post-Bonneville (^{14}C ages <7.5 ka). Pre–saline pan and saline pan sediments align with these distinct sample populations. Radiocarbon sample dates show one age inversion at the base of the pre-Bonneville record. That inversion may be attributable to decreased precision with nearly radiocarbon-dead samples (Table 2, samples 17 and 20). Pre-evaporite deposits (except for reworked sediments from unit II) date to before Lake Bonneville, and no ostracode species assemblages or stratigraphic features indicative of Lake Bonneville were detected. The progressively increasing age of sediments with depth indicates that our samples do not come from radiocarbon-dead (>50 cal ka BP) sediments. Furthermore, paired total inorganic carbon (TIC) and TOC measurements from the same depth (Table 2, samples 9 and 10) show similar date results, indicating that pre-Bonneville samples are not from radiocarbon-dead sediments (as we would anticipate variation in modern carbon contamination for TIC vs. TOC samples).

The age–depth models (Fig. 3) confirm the synchronous deposition of interpreted stratigraphic units. Even before stratigraphic correlations are used to increase age–depth model data density, interpreted depositional environments have similar ages across models. All pre-evaporite intervals exhibit comparable average depositional rates of around 20 cm/1000 yr. However, varying sediment thicknesses across the same units and unconformities suggest variations in depositional rates.

Stratigraphic units

We identified eight late Pleistocene to Holocene stratigraphic units. Units VIII to III are late Pleistocene, unit II is associated with the Pleistocene–Holocene transition, and unit I is Holocene. In addition to reporting the mean age–depth model ages of each stratigraphic unit, we report the maximum to minimum ages (95% confidence interval) of the top of each unit (Table 5). This shows the extent of uncertainty in age–depth models (Fig. 3).

https://doi.org/10.1017/qua.2023.79 Published online by Cambridge University Press

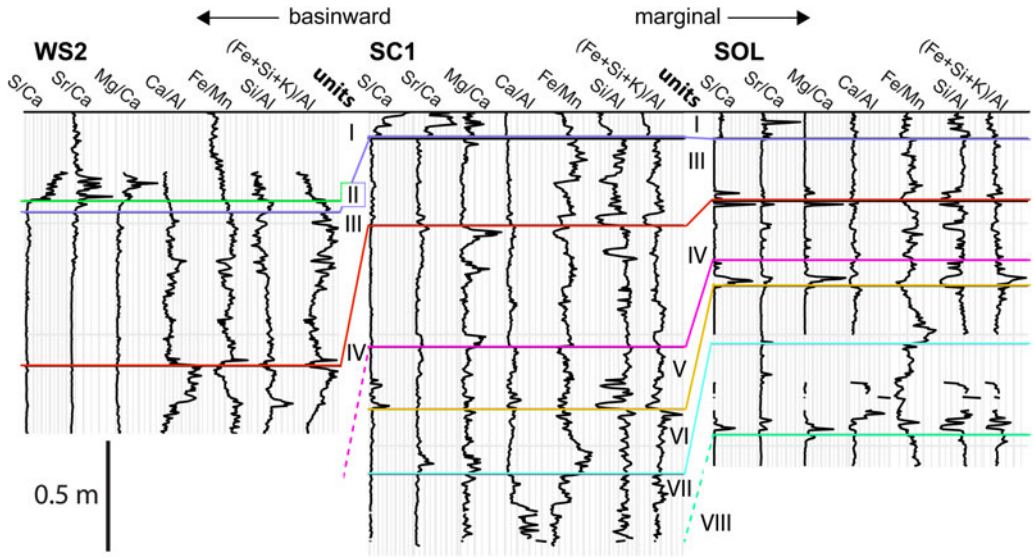

Figure 5. Portable X-ray fluorescence spectrometer (pXRF) elemental count ratio data for WS2, SC1, and SOL (cores penetrating the carbonate mud interval). Vertical scale consistent for all cores. Stratigraphic units are shown to highlight similarities and differences across cores. Blank areas on the cores denote areas where pXRF readings with no filter and He gas on were unsuccessful. pXRF data available in the Supplementary Data.

Unit VIII: Low-salinity saline lake

Unit VIII (>48 cal ka BP) consists of millimeter- to sub-millimeter-scale laminated aragonite marl. Unit VIII is only at the base of SOL (Fig. 4), with a thickness exceeding 27 cm (base not encountered). Unit VIII contains diatoms and ostracodes that decrease upward toward its top, indicating a transition to a lake with higher salinity.

Unit VII: Moderately to highly saline lake

Unit VII (48 to 45 cal ka BP) occurs at the base of SC1 (>65 cm thick) and near SOL's base (82 cm thick). Smear slides show that sediment near the base of unit VII contains low levels of aragonite (<25%) and a relatively elevated concentration of calcite and dolomite (<75%; Supplementary Data). XRD analysis of SOL sediments shows that the basal laminated part of unit VII consists of dolomite. The Mg/Ca ratio increases with elevated dolomite occurrence (Fig. 5). Unit VII contains trace, possibly detrital, ostracodes and diatoms (Fig. 4). The center of unit VII contains a mottled carbonate consisting of rod-shaped ooids and platy ooid aggregates. This mottled carbonate section has the highest Ca/Al ratio observed in SOL and SC1 (Fig. 5) and contains elevated (>50%) non-aragonite carbonates, which are interpreted here as dolomite and calcite because of high Mg concentrations in XRF data and increased evidence of dolomite and calcite in SOL XRD data. Ankerite also occurs in the mottled carbonate interval at the center of unit VII. The upper part of unit VII consists of aragonite-rich mud and is associated with a significant increase in the Fe/Mn ratio.

Mineralogical, microfossil, and elemental observations suggest that unit VII encompasses a moderately to highly saline lake falling water-level period, followed by a low water-level period, and a subsequent transition back to laminated, microfossil-poor aragonite mud depositional conditions.

Unit VI: Low-salinity saline lake

Unit VI (45 to 42 cal ka BP) occurs in the SC1 and SOL cores (58 and 52 cm thick, respectively). At the base of unit VI in SOL, a hard millimeter-thick calcite (XRD confirmed) layer is covered by a centimeters-thick dark-brown interval, indicating a rapid increase in detrital input and a change in water chemistry. The most diagnostic part of unit VI is a significant increase in ostracode and diatom occurrence (Fig. 4). Post–unit VI ostracode occurrences are much thinner in SC1 and SOL, indicating that unit VI represents the largest, longest-lived, or best-preserved low-salinity saline lake in BSF cores.

Unit VI is notable for having the highest Fe/Mn ratio of any unit (Fig. 5). This unit has higher concentrations of Al, Ti, Fe, and Si than other units, suggesting more detrital deposition relative to endogenic carbonate deposition, as would happen under deeper lake conditions. Al, Ti, and Si concentrations decrease at the top of unit VI, suggesting an increase in endogenic mineral deposition associated with a gradual water-level decline.

Unit V: Moderately to highly saline lake

The base of unit V (42 to 40 cal ka BP) is delineated by a transition from relatively high ostracode occurrence to ostracode absence (Fig. 4). Unit V is 56 cm thick at SC1 and 23 cm thick at SOL. This unit contains rod-shaped ooid sand beds and carbonate granules likely deposited in nearshore conditions. Unit V has a sand layer with low Al, Ti, Fe, and Si and a spike in S/Ca (Fig. 5), suggesting the presence of gypsum. SOL sediments show increased dolomite and suspect calcite deposition during this period. At the transition between units V and IV in SC1 and SOL, there is an unconformity and the Fe/Mn ratio drops.

Unit IV: Low-salinity saline lake

Unit IV (40 to 36 cal ka BP) is the deepest unit encountered at all primary coring locations (WS2, SC1, and SOL, where it is >62, 109, and 53 cm thick, respectively; Fig. 4). It consists of laminated aragonite-rich marls with a continuous ostracode-rich interval in WS2. Ostracodes and diatoms are intermittent in unit IV in SC1 and SOL.

Diatom abundance peaks in the middle of unit IV in WS2, indicating decreasing salinity during lower unit IV's deposition

https://doi.org/10.1017/qua.2023.79 Published online by Cambridge University Press

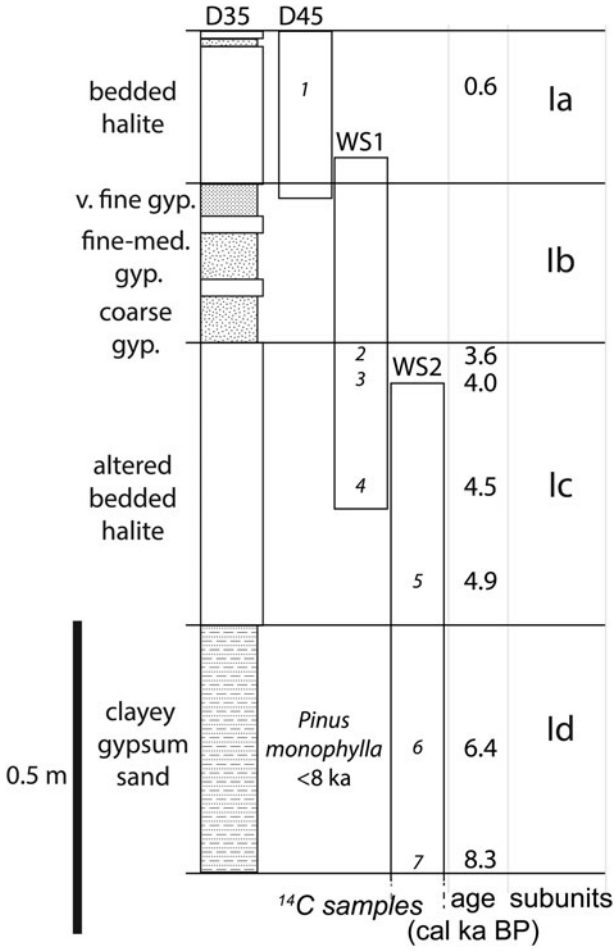

Figure 6. Stratigraphy and chronology of unit I (the evaporite interval) at the site of WS2/WS1. Radiocarbon sample numbers (1–7) shown for reference (Table 2). D45, collected from the southern section of the Bonneville Salt Flats (BSF) (Fig. 1B), is presented here with its corresponding subunit. The stratigraphy illustrated in Fig. 1C for WS2 aligns with the stratigraphy depicted here, initially described as core D35 by Bowen and others (2018b) and further detailed by Bernau and Bowen (2021). gyp., gypsum.

and increasing salinity during upper unit IV's deposition. Al, Ti, Fe, and Si also increase in the middle of unit IV (Fig. 5), suggesting that detrital deposition increased relative to endogenic carbonate deposition when the lake was at lower salinities.

In SC1 and SOL, the top of unit IV is very pale in color and has a spike in Mg/Ca before transitioning to unit III's basal sandy unit, indicating a rise in dolomite occurrence and endogenic deposition at the end of unit IV. In WS2, the contact between units IV and III is sharp, with a rapid decrease in ostracodes and a sudden shift to ooid-rich carbonate clumps, a near-lakeshore deposit. This transition suggests rapid drying and potentially an unconformable contact between units IV and III.

Unit III: Moderately to highly saline lake

Unit III (36 to >28 cal ka BP) consists of laminated to finely bedded marl and is consistent with a moderately to highly saline lake. Unit III is 138 cm thick at WS2, 78 cm thick at SC1, and 56 cm thick at SOL. Non-detrital ostracodes do not occur, and diatom abundance is low (Fig. 4). Dates from the younger portion of this unit (Table 2, radiocarbon samples 9 and 10) suggest an age corresponding to early Lake Bonneville (<30 cal ka BP); however, unit III's saline sediments are not consistent with the freshwater units containing *L. staplini* with finely laminated algal marls deposited by early Lake Bonneville, indicating dates from samples 9 and 10 are younger than they should be given their stratigraphic context or that further refinement of early lake Bonneville sediment ages is needed. Refinement of Lake Bonneville's early chronology based on these samples alone is not justified, as they are limited in number and have several dating uncertainties.

Unit III in SC1 and mid–unit III in WS2 have orange tinting, indicating oxidation. Several small sandy layers in WS2 and larger sandy layers in SOL and SC1 indicate periods with more nearshore deposition with shallower water depths. (Fe + Si + K)/Al and Si/Al drop at the base of unit III with a sandy bed (Fig. 5). Si/Al declines in the upper part of WS2 but not in SC1/SOL, suggesting lateral depositional differences or erosion of the upper part of unit III at SC1 and SOL. The contact between unit III and overlying sediments (unit I or II) appears as a shift from finely bedded, lighter-colored carbonate mud to a massive, darker, muddy layer (unit II) in WS2 or as an abrupt change from finely bedded carbonate mud to coarse gypsum sand (unit I) in SOL and SC1.

Unit II: Reworked deposits

Unit II (<13 to 8.3 cal ka BP) consists of poorly bedded carbonate mud and only occurs at WS2 (10 cm thickness; Fig. 4). Unit II sieved samples processed for ostracodes contained only rod-shaped ooids. Poor agreement between model age and sample age for unit II's radiocarbon sample (sample 8 in Fig. 3C and Table 2) indicates an unconformity between units II and III at WS2. Given this unconformity and the absence of sediments that are consistent with Lake Bonneville in microfossil assemblage and sedimentological characteristics, this unit was likely deposited during post-Bonneville time (<13 cal ka BP), potentially from a mix of contemporary and reworked pre-Bonneville sediments or reworked Lake Bonneville marls.

Unit I: Saline pan

Unit I (8.3 cal ka BP to modern) consists of saline pan sediments that are 137 cm thick at the site of WS2 (and 22 and 24 cm thick at SC1 and SOL, respectively). Unit I consists of four laterally discontinuous subunits (Figs. 1C and 6). Sediments at the saline pan center (WS2) are thickest and thin to the edges. We examined shallow cores collected in 2016 and found that saline pan sediments on the edge of BSF contain more ooids (reworked in origin) than other BSF locations, indicating higher detrital constituents. Here, we describe sediments from the center of the saline pan (WS2 and WS1), which have the least dissolved and thickest evaporite deposits. The high porosity and uneven surface of bedded evaporite layers cause the pXRF data quality to vary in unit I. In pXRF data, unit I is differentiated from underlying carbonates by Cl/Br, S/Ca, and Sr/Ca ratios (Fig. 5).

The basal saline pan layer (Fig. 6, subunit Id; 8.3 to 5.4 cal ka BP) consists of gypsum sand with carbonate mud and is 40 cm thick. We did not identify the Mazama ash (7.7 cal ka BP; Egan et al., 2015) in subunit Id, although it occurs in the nearby Juke Box trench as a 0- to 3-cm-thick interval (Oviatt et al., 2018). *Pinus monophylla* pollen, which first appeared in the Bonneville basin around 8 cal ka BP (Madsen and Rhode, 1990), is present in subunit Id, consistent with our radiocarbon ages. The extent of subunit Id is limited to the saline pan center (Fig. 1C).

Subunit Ic (5.4 to 3.5 cal ka BP) is a 46-cm-thick, altered bedded halite layer. The altered bedded halite indicates a shallow

https://doi.org/10.1017/qua.2023.79 Published online by Cambridge University Press

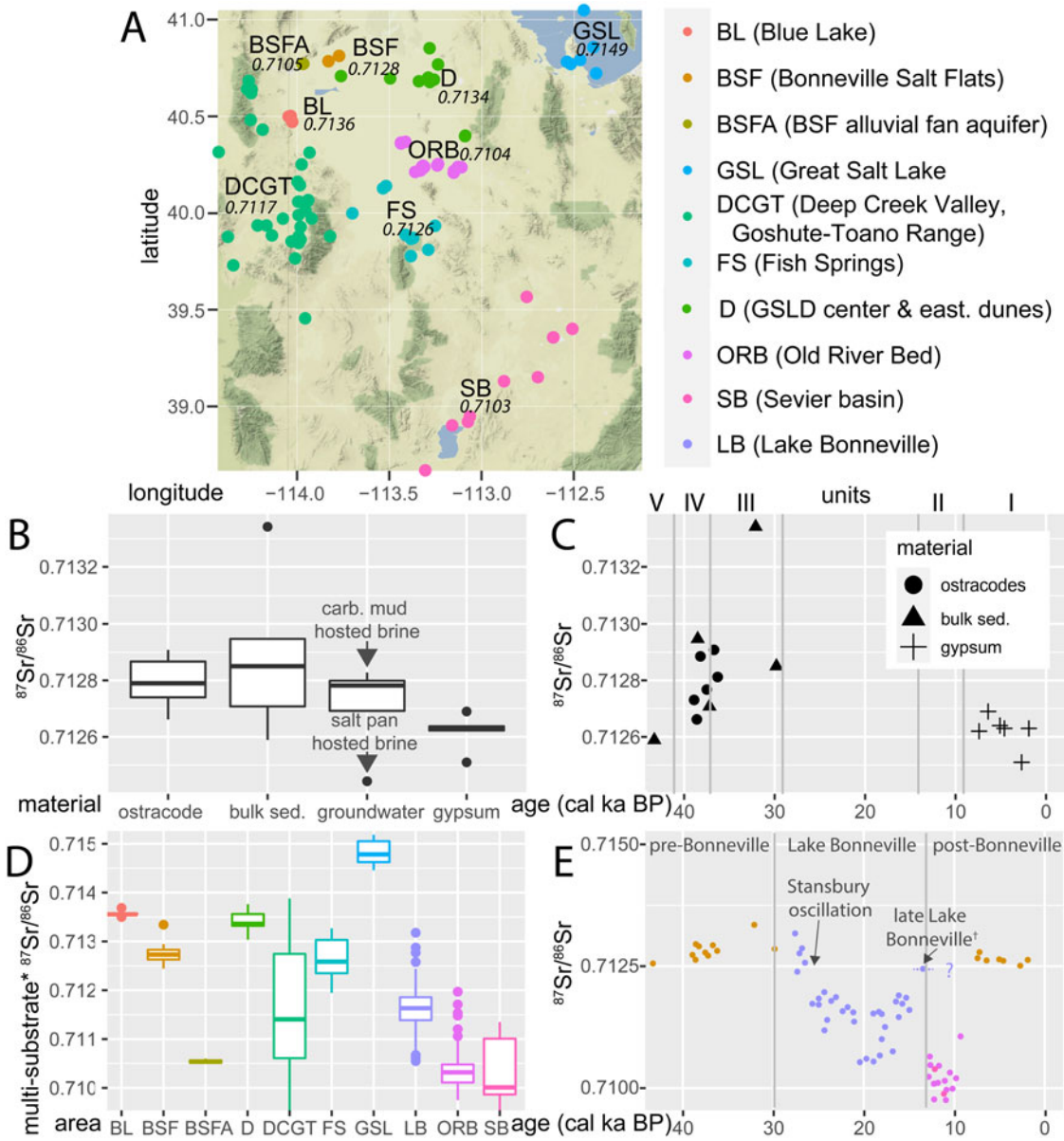

Figure 7. $^{87}Sr/^{86}Sr$ ratios from Bonneville Salt Flats (BSF) sediments and water in comparison with regional multi-substrate values. (**A**) Sample locations with mean local $^{87}Sr/^{86}Sr$ ratio from multiple substrates in italics. Base map from OpenStreetMap. (**B and C**) BSF saline pan sample results by (**B**) sample type and (**C**) sediment age. Multi-substrate $^{87}Sr/^{86}Sr$ ratios by (**D**) area and (**E**) over time (Tables 3 and 4). Data compiled by area, measured material, and location are available in the Supplementary Data.

(**D**) Multi-substrate: Measured substrates consist of near-surface sediments, shells, spring water, ground water, and surface water from streams and small spring-fed lakes. Except for elevated stream water $^{87}Sr/^{86}Sr$ ratios (0.002 higher than ground water and spring water on average) in the Deep Creek Valley and Goshute-Toano Range, surface, spring-water, and groundwater $^{87}Sr/^{86}Sr$ for each area were very similar (<0.0003 difference on average). In addition to shells, near-surface sediment samples consisted primarily of endogenic sediments and are interpreted to be indicative of water sourcing at the time of mineral precipitation. (**E**) Samples denoted by a dagger (†) identified as Gilbert episode in Hart et al. (2004). However, given poor chronological constraint on sample material, measurements may represent late Lake Bonneville $^{87}Sr/^{86}Sr$ ratios.

saline depositional environment where halite crystallized in situ from surface water and was later altered by dissolution and secondary halite growth (Bernau and Bowen, 2021). Subunit Ic is more extensive and thicker than subunit Id. Subunit Ic's higher depositional rate compared with subunit Id indicates that halite deposition may have been relatively rapid.

Gypsum sand with small halite beds (subunit Ib: 3.5 to 1.7 cal ka BP; 26 cm thick) covers subunit Ic. Subunit Ia (1.7 cal ka BP to present; 25 cm thick) is a surficial halite layer with thin gypsum layers. A TOC sample from the site of the thickest subunit Ia deposition (D45; Fig. 1B) indicates 8 (±2) cm of halite deposition since ~600 cal BP.

DISCUSSION

Pre-Bonneville saline lakes (stratigraphic units VIII–III)

The lacustrine sediment underlying BSF originates from a carbonate-precipitating, ostracode-supporting, low salinity, saline lake to a high-salinity lake that intermittently occurred from

https://doi.org/10.1017/qua.2023.79 Published online by Cambridge University Press

Table 3. $^{87}Sr/^{86}Sr$ isotope ratio data from core samples collected from the Bonneville Salt Flats, Utah, USA.[a]

Core	Core depth (cm)	Depth below surface[b] (cm)	$^{87}Sr/^{86}Sr$	Standard error (1σ)	Age (cal ka BP)	Type[c]
D35	28	28	0.71263	0.00001	1.9	Gypsum
D35	47	47	0.71251	0.00001	2.7	Gypsum
D35	79	79	0.71263	0.00001	4.6	Gypsum
WS2	34	88.5	0.71264	0.00001	5.1	Gypsum
WS2	60	114.5	0.71262	0.00001	6.4	Gypsum
WS2	80	135	0.71269	0.00001	7.4	Gypsum
WS2	110	165	0.71285	0.00000	29.8	Bulk sed.
WS2	150	205	0.71334	0.00000	32.1	Bulk sed.
WS2	238	293	0.71281	0.00001	36.3	Ostracodes
WS2	247	302	0.71291	0.00000	36.7	Ostracodes
WS2	258	313	0.71271	0.00000	37.2	Bulk sed.
WS2	263	318	0.71277	0.00001	37.5	Ostracodes
SC1	165	175	0.71289	0.00001	38.2	Ostracodes
WS2	283	338	0.71295	0.00001	38.5	Bulk sed.
WS2	285	340	0.71266	0.00001	38.6	Ostracodes
WS2	290	345	0.71273	0.00001	38.9	Ostracodes
SC1	274	284	0.71259	0.00000	43.3	Bulk sed.

[a]Samples are ordered from youngest to oldest. Measurements made at the University of Utah Earth Core Facility.
[b]Depth below surface does not correct for sediment compaction.
[c]Gypsum samples are post-Bonneville, ostracode and bulk sediment samples are pre-Bonneville.

>45 to >28 cal ka BP (Fig. 8B). Eardley (1962) previously published ^{14}C dates of bulk carbonates south of BSF, which are consistent with our chronology. Our chronology also aligns with the amino acid–racemization geochronology of *L. staplini* ostracodes from the Wendover core south of BSF, which were interpreted to be slightly older than Lake Bonneville sediments because of dating uncertainties and stratigraphic relationships (Bright et al., 2022).

The plate- and granule-shaped ooid aggregates at the center of unit VII are unique and did not appear in any other unit. This

Table 4. $^{87}Sr/^{86}Sr$ isotope ratio data from gypsum from Great Salt Lake Desert (GSLD) dunes.[a]

Sample ID	$^{87}Sr/^{86}Sr$	Latitude (°N)	Longitude (°W)
Solar Pond 1[b]	0.71376	40.769	113.236
Solar Pond 1	0.71359	40.769	113.236
Knolls 1	0.71329	40.679	113.280
East Knolls 1	0.71335	40.691	113.258
Knolls 2 SE 3	0.71304	40.853	113.282
West Knolls 2	0.71335	40.683	113.339
Salduro 3	0.71336	40.709	113.761
Salduro 3 duplicate	0.71339	40.709	113.761
Barro 3	0.71359	40.698	113.495

[a]Medium sand grains (<300 and >150 μm in diameter) were analyzed (unless otherwise noted). Measurements made at the University of Utah Earth Core Facility. Standard error for all samples (1 σ) is 0.00001. Samples are described in Boden (2016). Latitude/longitude data are WGS84.
[b]Bulk sediment sample.

Table 5. Ages of tops of stratigraphic units.[a]

Stratigraphic unit	Age of unit top (cal ka BP)	Maximum/ minimum age (cal ka BP), 95% confidence interval	Age of unit base (cal ka BP) if base differs from the top of the underlying unit[b]
VIII	>48	46/50	Base not encountered
VII	45	42/48	
VI	42	40/45	
V	40	38/42	
IV	36	34/38	
III	>28[c]	27/29	
II	8.3	8.1/8.4	<13[d]
Id	5.4	5.1/5.9	
Ic	3.5	3.4/3.7	
Ib	1.7	1.2/2.4	
Ia	Present (<0.6[e])	<0.5/<0.7	

[a]Mean age–depth models' age and 95% confidence interval maximum and minimum age of unit tops noted. Note that this uncertainty does not include unknowns related to modern atmospheric carbon contamination, reworked carbon, or radiocarbon reservoir effects.
[b]There may be unconformities that were not resolvable given sample collection frequency and sample error (specifically within and at the base of units VII, V, and III).
[c]Because unit III sedimentological differs from Lake Bonneville stratigraphy, the top of unit III is interpreted as older than early Lake Bonneville (<30 cal ka BP).
[d]Unit II age is interpreted based on stratigraphic context (post–Lake Bonneville to before unit I).
[e]At least 8 (±2) cm of halite deposited since 0.6 cal ka BP.

https://doi.org/10.1017/qua.2023.79 Published online by Cambridge University Press

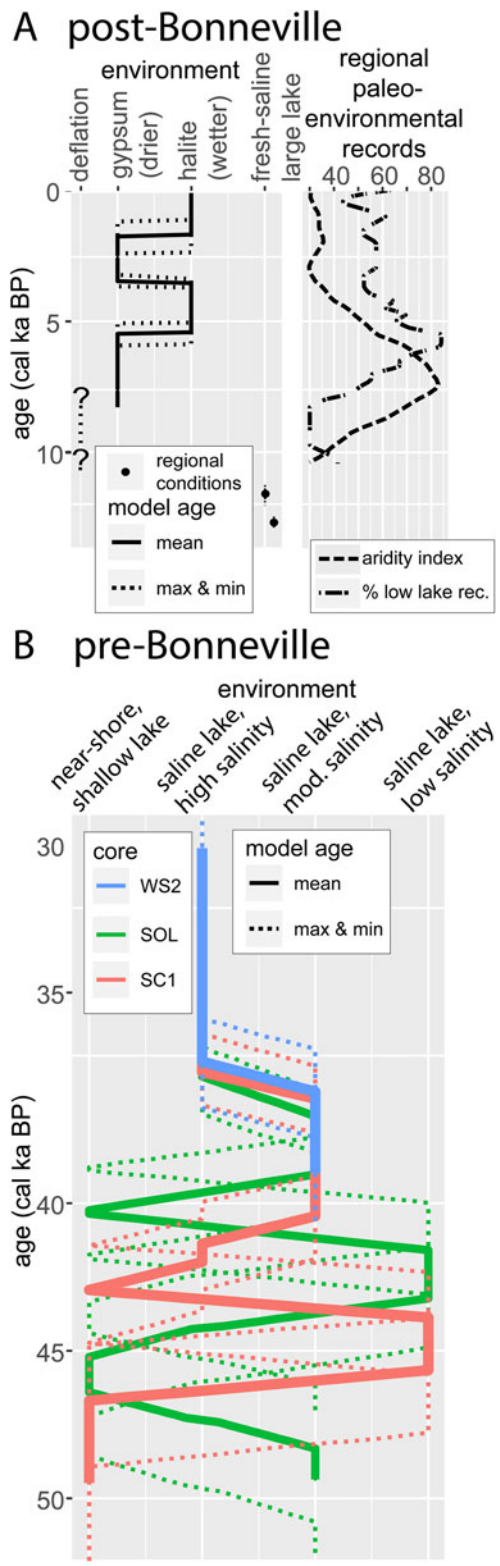

Figure 8. Summary of depositional conditions at the Bonneville Salt Flats (BSF) over time. (**A**) Post-Bonneville saline pan stage showing trends in relative water inputs over the past 8000 yr in comparison with regional paleoenvironmental records. These records include an aridity index of the southwestern United States (Lachniet et al., 2020) and a record of Great Basin lakes at low levels (Steponaitis et al., 2015). Post-Bonneville depositional conditions before BSF deposition noted with black dots (Old River Bed delta lake, the Gilbert episode, and deflation) (Oviatt, 2014; Palacios-Fest et al., 2021). (**B**) Pre-Lake Bonneville depositional environments interpreted from BSF cores. Discrepancies in lake history records between cores in **B** rise due to variations in the age–depth models of the cores (Fig. 3).

aggregate layer is consistent with partially exposed cemented beach or microbial mat–stabilized deposits similar to modern GSL near-lakeshore platy carbonates, which also have elevated endogenic dolomite concentrations (Burke and Gerhard, 2000; Yucel et al., 2020). Ankerite in the plate- and granule-shaped ooid aggregate layer suggests microbially assisted precipitation, supporting a microbial-influenced origin interpretation (Morad, 1998; Ulmer-Scholle et al., 2014).

The absence of gypsum sand beds, or other features suggestive of saline pan deposition in pre-Bonneville units, indicates pre-Bonneville saline pans did not exist or were not preserved in the cores. Unconformable contacts between sandy nearshore deposits and underlying low to moderate-salinity saline lake deposits suggest periods of desiccation and deflation.

The pre-Bonneville shallow saline lakes at BSF varied in salinity over time. Differences in unit thickness between SC1 and SOL cores near the edges of BSF, and WS2 near the depocenter (Fig. 4), suggest that the shallow lake varied from extending over much of GSLD (when it was relatively less saline) to being locally restricted (when it became highly saline). In most lake settings, sedimentation is anticipated to be thicker at the basin's edge and thinner at its sediment-starved center. However, we see the opposite pattern at BSF. We propose that the differences in sedimentation rates in pre-Bonneville sediments at BSF reflect lateral changes in erosion and, correspondingly, sediment preservation. This pattern may also be attributed to differences in sediment source, which is primarily endogenic at BSF compared with more detrital influence in other settings. During low lake levels, indicated by high salinity and nearshore sand deposition, the basin's edge experienced increased exposure and was more susceptible to erosion. Meanwhile, areas near the depocenter had minimal erosion and potentially saw enhanced deposition from eroded sediments. Low lake-level conditions occurred several times in the pre-Bonneville record, contributing to the thinning of units on the edge of the shallow lake. Under fresher, deeper-water conditions, as occurred during unit VI, deposition was relatively constant at SOL and SC1. Unit IV depositional conditions seem more variable than those for unit VI, with the ostracode record in unit VI in SOL and SC1 showing intermittent periods of non-ostracode deposition. In contrast, the ostracode record in unit IV was continuous (Fig. 4). The intervals of non-ostracode deposition in unit IV at SC1 and SOL indicate periods of lower water levels. In addition to this evidence for unconformities, unidentified paraconformities may also exist.

Relatively constant $^{87}Sr/^{86}Sr$ ratios from pre-Bonneville ostracodes and carbonate sediment (Fig. 7B, C, and E) indicate that water provenance did not change significantly during the period of unit V to unit III. $^{87}Sr/^{86}Sr$ ratios in saline lake sediments are most consistent with local ground water ($^{87}Sr/^{86}Sr$: 0.7127) and late Lake Bonneville water and pre-Stansbury oscillation water ($^{87}Sr/^{86}Sr$: 0.7124 and 0.7128, respectively; Fig. 7E), when a shallow lake connected GSLD and GSL (Hart et al., 2004; Pedone and Oviatt, 2013; Lerback et al., 2019; Munroe et al., 2019; Carling et al., 2020; Bradbury et al., 2020; Palacios-Fest et al., 2021). The similarity of $^{87}Sr/^{86}Sr$ ratios in pre-Bonneville sediments and the ground water they host (Lerback et al., 2019) imply a source in common, or groundwater strontium isotope ratios are in equilibrium with sediment strontium isotope ratios.

Monospecific *L. staplini* assemblages in the Bonneville basin were previously interpreted as indicative of a shallow (~15- to <80-m-deep) saline lake with water levels between ~1300 and <1380 m elevation (similar to early Lake Bonneville as it rose to

https://doi.org/10.1017/qua.2023.79 Published online by Cambridge University Press

Stansbury oscillation levels; Oviatt, 2017; Fig. 2). If pre-Bonneville conditions were consistent with early-Bonneville conditions, then the pre-Bonneville *L. staplini*–supporting lake would have surpassed the current 1285 m threshold between GSL and GSLD (Oviatt et al., 2021; Fig. 2). These observations support the interpretation that pre-Bonneville low-salinity saline lakes connected GSL and GSLD.

Regional records show the pre-Bonneville climate was relatively dry but cooler than today, with shallow, intermittently expansive lakes, broadly corresponding to our observations of pre-Bonneville deposits from BSF (Rhode, 2016; Thompson et al., 2016). Similar to BSF, the location of GSL had shallow ostracode-supporting saline lakes with periods of desiccation from 45 to 30 cal ka BP (Balch et al., 2005; Thompson et al., 2016). Holocene GSL has no records of ostracodes, indicating that the pre-Bonneville lake at the location of GSL was intermittently less saline than Holocene GSL.

Post-Bonneville unconformity and reworked deposits (unit II)

We did not find evidence of Lake Bonneville sediments above units VIII to III, suggesting that local erosion may have caused their disappearance. Previous examination of cores and exposures around GSLD reveals that Lake Bonneville sediments thin toward the saline pan and are absent at and near BSF (Oviatt et al., 2020; Bernau et al., 2023). This deflationary trend reflects changes in elevation, with higher basin-floor areas having better sediment preservation than lower areas. The post-Bonneville depositional record enables us to test our hypotheses that (1) the saline pan formed as climate shifted from wet to arid (these conditions were met when Lake Bonneville desiccated) or (2) that BSF formed when climate shifted from highly arid to wet. BSF's depositional history reveals non-deposition and erosion following Lake Bonneville, disproving our first hypothesis and invalidating the long-held presumption that BSF formed from the desiccation of late Pleistocene Lake Bonneville. Instead, a playa, consisting of lacustrine mud (a mudflat), likely formed after Lake Bonneville.

Wind erosion removed Lake Bonneville sediments from BSF between 13 and ~8.3 cal ka BP. Several lines of evidence indicate Lake Bonneville sediment was removed by deflation: (1) Lake Bonneville sediment is eroded across GSLD, with Lake Bonneville sediment thinning toward and then becoming absent at BSF (Bernau et al., 2023). (2) BSF is a GSLD topographic low point; if sediments were removed by water, they would have been deposited at BSF. (3) Jones (1953) interpreted the origin of GSLD gypsum dunes as resulting from the deflation of surficial sediments, indicating historical surface deflation of the GSLD playa.

Deflation from a playa's surface occurs when groundwater levels fall due to increasing aridity (Jacobson, 1988; Rosen, 1994; Cahill et al., 1996; Dutkiewicz et al., 2000; Reynolds et al., 2007). Under Rosen's hydrological framework (1994), past BSF deflation suggests it was a recharge playa through which ground water was recharged and transported elsewhere. Alternatively, deflation indicates a system at disequilibrium with its current climate conditions. Post-Bonneville GSLD's hydrology likely became open only when a shallow lake connected GSLD and GSL. Otherwise, it was a discharge playa, with water being removed by evaporation. Therefore, it is likely that when deflation occurred at BSF, it was because BSF's surface was not at equilibrium with climate.

Analysis of modern desiccating saline lakes indicates that, depending on groundwater levels and salinity, saline ground water may enhance or limit deflation (Cahill et al., 1996; Reynolds et al., 2007). Low salinity and low groundwater levels can stabilize surface sediments, creating hard cemented crusts (Fig. 9). Although deflation occurred at various GSLD locations, Lake Bonneville sediments persist in many areas (Bernau et al., 2023). The persistence of Lake Bonneville sediments in the elevated regions around BSF could be attributed to low salinity and low groundwater-level conditions leading to the past formation of hard cemented crusts.

Researchers have determined that mudflat deflation increases as the groundwater capillary fringe reaches the surface, triggering groundwater evaporation and efflorescent crust formation (Cahill et al., 1996; Reynolds et al., 2007; Fig. 9). Efflorescent crusts are the most erodible basin-floor land cover, as they are easily broken, creating abrasive particles that enhance deflation. Repeated removal of Na^+ and Cl^- ions from ground water over multiple cycles of efflorescent halite growth and deflation may have enriched ground water at BSF with potassium, contributing to this site's presently mined potassium resources. Groundwater evaporation also enables displacive minerals, commonly gypsum, to grow in the capillary zone, further destabilizing near-surface

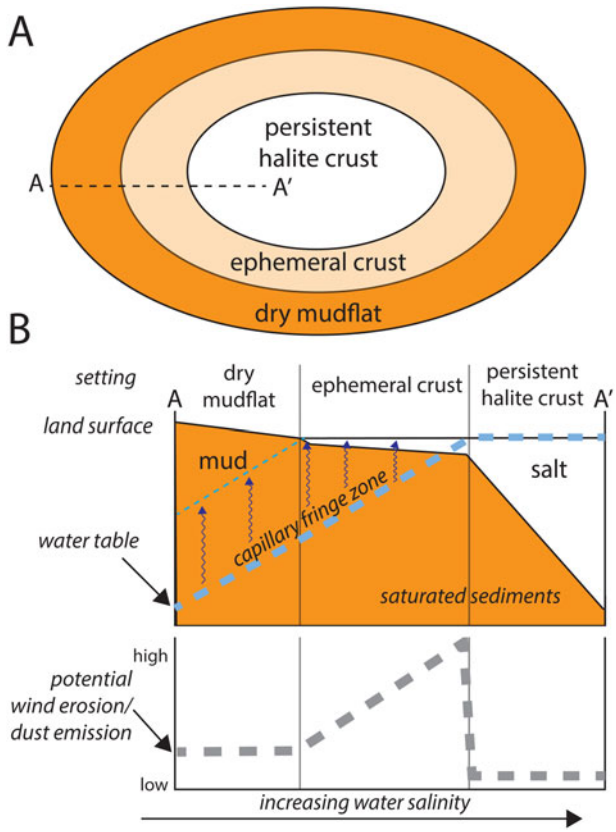

Figure 9. Deflationary model for the Bonneville Salt Flats (BSF) area. (**A**) Map view of spatial distribution of surface material with the saline pan at its center. (**B**) Cross section of A–A′. Bottom part shows changes in potential wind erosion with increasing salinity. Erosion is low at the mudflat under low-salinity, low groundwater-level conditions. As groundwater levels rise, introducing the capillary zone to the surface, erosion intensifies, giving rise to highly erodible ephemeral crusts. Ultimately, erosion diminishes with the establishment of a persistent halite crust, supported by high groundwater levels and regular surface flooding. Figure modified from Bernau et al. (2023) and is based on information from Reynolds et al. (2007).

https://doi.org/10.1017/qua.2023.79 Published online by Cambridge University Press

sediments (Rosen, 1994; Kocurek et al., 2007). Highly saline surface water can lead to the formation of erosion-resistant bedded evaporites. Deflation likely ceased as bedded halite deposits formed in saline ponded water supported by high groundwater levels and precipitation. After halite deposition began at the saline pan center, the saline pan edge area still consisted of erodible efflorescent crusts (Fig. 9A), as it does today, and deflation of peripheral efflorescent crusts possibly contributed to the relative thinness of unit III at SC1 and SOL.

Within this framework, where deflation or deposition is controlled by water level and salinity, the cessation of deflation at BSF suggests either (1) groundwater levels fell below the capillary fringe in the past, enabling a cemented mud crust to form, which is unlikely given BSF's location as a drainage terminus; or (2) that groundwater levels were high enough to support the accumulation of salts and the formation of bedded evaporites after surface water was present. High groundwater levels could have resulted from increased precipitation or lower evaporation rates. The modern presence of a salt crust at BSF suggests that a shift to a wetter climate likely triggered the formation of the crust.

Regional and local records indicate a highly arid period from 9 to 5 cal ka BP (peak aridity ~7.5 cal ka BP; Fig. 8A) (Louderback and Rhode, 2009; Steponaitis et al., 2015; Lachniet et al., 2020). Deflation of 1 to 2 m of Lake Bonneville sediments at BSF's site may have occurred early in this period. Before this time, the Old River Bed in the southern GSLD (through which post-Bonneville Sevier basin water drained to GSLD; Fig. 7A and E) was relatively wet (13 to ~9.5 cal ka BP), varying from preserving evidence of a brief freshwater lake (that connected GSL to GSLD, thus inundating the BSF area) to an extensive wetland with some periods of higher aridity, suggesting that there was likely limited GSLD deflation at that time (Oviatt et al., 2003; Madsen et al., 2015; Bradbury et al., 2020; Palacios-Fest et al., 2021). Because of flooding, there was no erosion at BSF during the Gilbert episode (11.6 cal ka BP; Fig. 8A).

Some deflated sediments were redeposited at BSF before gypsum deposition occurred. The disparity between the depositional environment of unit II sediments (poorly bedded carbonate mud with rod-shaped ooids), which demonstrate a saline setting, and their apparent Lake Bonneville age (24 cal ka BP; Table 2, sample 8) indicates dates are not reflective of depositional timing, suggesting sediment reworking. A Lake Bonneville age is only possible for unit II sediments if the age is incorrect or if sediments are reworked Lake Bonneville sediments (or pre-Bonneville mixed with post-Bonneville sediments) that were deposited after Lake Bonneville desiccated (<13 cal ka BP) but before the onset of gypsum deposition (>8.3 cal ka BP).

Saline pan (unit I)

The area of former deflation at BSF became a depocenter with evaporite accumulation at 8.3 cal ka BP. Deposition of basal muddy gypsum sediment (8.3 to 5.4 cal ka BP) in subunit Id coincides with rising to elevated regional aridity (Steponaitis et al., 2015; Lachniet et al., 2020). Blue Lake, a wetland system located ~30 km south-southwest of BSF on the edge of the GSLD basin (Fig. 7A), had a pronounced desiccation period from 8.3 to 6.5 ka (Louderback and Rhode, 2009). GSL was saltier at this time (7.2 to 5.5 cal ka BP; So et al., 2023). A compilation of Great Basin lakes showed an increasing proportion of lakes at low levels from 8 to 6 cal ka BP; lakes generally became deeper after 5.5 cal ka BP (Steponaitis et al., 2015). Similarly, records from the Estancia Basin, New Mexico, indicate deflation contemporary with BSF gypsum deposition from 7.0 to 5.4 cal ka BP, followed by a water table rise (Menking and Anderson, 2003), paralleling BSF's record of changing water availability.

The model in Figure 9 suggests that deflation ceased at BSF when a bedded evaporite crust formed. However, no preserved bedded evaporite crust is found at the base of subunit Id. This suggests either (1) a crust formed and later dissolved, or (2) in the absence of a bedded evaporite crust, the accumulation of gypsum grains alone was enough to halt deflation.

Past petrographic observations indicate that BSF gypsum includes authigenic and detrital grains, but the primary gypsum source remained undetermined (Bowen et al., 2018a; Bernau and Bowen, 2021). Gypsum crystals at the saline pan base are the largest and most euhedral, whereas near-surface crystals are fine-grained and rounded. Researchers interpreted these grain sizes and shapes as evidence of diagenetic growth on emplaced crystals and the reworking of more recent crystals. BSF saline pan–edge sediments are more strongly influenced by detrital deposition than BSF center sediments, with edge sediment having higher concentrations of ooids. BSF gypsum sand differs from GSLD gypsum dunes to the southeast and east of BSF. GSLD gypsum dune sediments are finer, with rounded abraded grains and higher non-gypsum constituents (>30% ooids in some dunes; Jones, 1953). GSLD gypsum dune $^{87}Sr/^{86}Sr$ ratios indicate distinct sediment sourcing compared with BSF (Fig. 7A, B, and D; Tables 3 and 4), suggesting BSF's gypsum is primarily authigenic and locally reworked.

As a terminus for the southern GSLD watershed, BSF is a discharge playa for regional groundwater flow. There is little evidence of upwelling immediately beneath the saline pan (Lines, 1979; Mason and Kipp, 1998). Previous work suggests that BSF ground water may partly originate from the upwelling of thermal water moving along faults in the Wendover Graben (Smith et al., 2012). Additionally, modern hydrological studies of groundwater discharge from similar desert playas indicate that playa discharge is minimal, accounting for less than 2% of drainage area discharge, with much basinal discharge occurring at the interface between alluvial fan and playa sediments (Jackson et al., 2018). These hydrological findings emphasize the importance of a regional approach in comprehending groundwater discharge in this area. Surface and near-surface water transported near-surface salts (that formed through groundwater evaporation) to the saline pan over time.

Lerback et al. (2019) determined that water hosted in BSF saline pan evaporite sediments has a lower $^{87}Sr/^{86}Sr$ ratio ($n = 1$) than water hosted in underlying pre-Bonneville carbonate mud ($n = 3$; Fig. 7B). Gypsum $^{87}Sr/^{86}Sr$ ratios indicate BSF gypsum originates authigenically from underlying lacustrine sediment–hosted ground water mixed with evaporite-hosted water (groundwater in Fig. 7B). If the $^{87}Sr/^{86}Sr$ ratio of the lacustrine sediment–hosted aquifer is constant, the lower $^{87}Sr/^{86}Sr$ ratio in saline pan water suggests that, besides the ground water beneath the pan, a water source with a lower $^{87}Sr/^{86}Sr$ ratio is flowing into BSF. Possible lower $^{87}Sr/^{86}Sr$ ratio sources include nearby alluvial-fan water, the Old River Bed and Fish Springs to the south, and Deep Creek Valley and the Goshute-Toano Range to the southwest (BSFA, ORB, FS, and DCGT on Fig. 7D, respectively). Elevated $^{87}Sr/^{86}Sr$ ratios in water from Blue Lake, the largest active spring near BSF, indicate that Blue Lake and other more distant water sources have a minor influence on BSF water. Nearby alluvial-fan water, graben-associated spring flow (unknown $^{87}Sr/^{86}Sr$ ratios), and

https://doi.org/10.1017/qua.2023.79 Published online by Cambridge University Press

overland flow of rainwater-sourced water are the most likely sources of additional BSF water.

$^{87}Sr/^{86}Sr$ ratios of modern saline pan–hosted water may be altered by human activities. Since 1917, the extraction of near-surface saline pan–hosted water may have led to the upwelling of carbonate mud–hosted ground water and increased $^{87}Sr/^{86}Sr$ ratios of saline pan–hosted ground water. Past discharge from now-dormant springs may have depressed local $^{87}Sr/^{86}Sr$ ratios. Starting in 1998, alluvial-fan ground water with low $^{87}Sr/^{86}Sr$ ratios (0.7105; Lerback et al., 2019) has been introduced to BSF, possibly lowering $^{87}Sr/^{86}Sr$ ratios in evaporite-hosted water.

BSF's basal halite layer (subunit Ic) was deposited in a saline pan or saline lake with persistent to intermittent surface ponding from 5.4 to 3.5 cal ka BP (Fig. 8A). Regionally, this period shows declining aridity (Steponaitis et al., 2015; Lachniet et al., 2020). The timing of this increase in moisture aligns with a GSL shift to wetter conditions and lower salinities at 5.5 cal ka BP (So et al., 2023). This observation supports our second hypothesis that the saline pan (in its halite-depositing state) formed as the climate shifted from arid to wet. The depositional record from Blue Lake also indicates a relatively cool climate at this time (4.4 to 3.4 cal ka BP; Louderback and Rhode, 2009).

The shift from halite (subunit Ic) to gypsum sand (subunit Ib) suggests aridification, resembling conditions during the deposition of gypsum-rich subunit Id. This indicates an increase in eolian-available sediment and a simultaneous decrease in halite deposition from 3.5 to ~1.7 cal ka BP (Fig. 8A). Drier conditions may have caused lower groundwater levels, allowing rainwater to dissolve surficial halite. Gypsum that crystallized in the halite's interstitial pores would be exposed and accumulate into layers due to this dissolution process. Similarly, decreased groundwater levels would have enabled increased sediment reworking and transport and later deposition of detrital eolian gypsum. The lower part of subunit Ib coincides with a warm period in the Blue Lake depositional record from 3.4 to 2.7 cal ka BP (Louderback and Rhode, 2009). Furthermore, multiple records indicate an extended drought across the central Great Basin from 2.5 to 1.9 cal ka BP (Mensing et al., 2013).

The uppermost surface halite layers with small gypsum beds (subunit Ia) suggest variable deposition of gypsum and halite since ~1.7 cal ka BP, possibly from variability in aridity or local shifts in detrital gypsum deposition. Petrographic observations of subunit Ia sediments record a saline pan that varied between periods of flooding and desiccation (Bernau and Bowen, 2021).

Observations of modern processes at BSF yield additional insights into this system. Dust trap measurements indicate a possible modern eolian depositional rate of 30 cm/1000 yr (assuming sediment is not further reworked and modern rates are consistent with past rates; Bernau and Bowen, 2021). At this rate, if entirely detrital, the ~1-m-thick gypsum sequence at BSF's center would have been deposited in ~3000 yr.

Our data allow us to assess whether BSF is a significant sediment source for GSLD dunes. Modern observations indicate GSLD dune systems are mobile, with eastward movement (>1 km in some areas) occurring in the Knolls dune field from 1953 to 1972 (Fitzgerald, 2019). Remote sensing also detected the northeast movement of GSLD gypsum dunes between 1986 and 2016, suggesting winds coming from the direction of BSF (Radwin and Bowen, 2021). However, our measurements of gypsum $^{87}Sr/^{86}Sr$ ratios from GSLD gypsum dune sand to the east and southeast of BSF indicate that the impact of BSF gypsum, if present, is negligible on GSLD gypsum dunes. High $^{87}Sr/^{86}Sr$ ratios in GSLD gypsum dunes suggest the water contributing to the gypsum likely came from the remnants of a period of connectivity between GSL and GSLD through a shallow lake, possibly during the late phase of Lake Bonneville or the Gilbert episode (Fig. 7D and E).

CONCLUSIONS

Observations from sediment cores spanning BSF facilitate a new interpretation of deposition and erosional history of the western GSLD spanning the late Pleistocene to the modern. BSF's site hosted shallow lakes with varying salinity intermittently from >45 to >28 cal ka BP. $^{87}Sr/^{86}Sr$ ratio measurements from pre-Bonneville sediments align with $^{87}Sr/^{86}Sr$ ratios from early Lake Bonneville and the late lake-level falling phase of Lake Bonneville. $^{87}Sr/^{86}Sr$ ratios in pre-Bonneville BSF sediments and ostracode occurrence limited to *L. staplini* suggest pre-Bonneville lake water levels were high enough to connect GSLD and the site of GSL multiple times between >45 to >28 cal ka BP.

Despite BSF being a regional depocenter since the Miocene (Miller et al., 2021; Bernau et al., 2023), Lake Bonneville sediments are absent at BSF, indicating that BSF did not form from the desiccation of Lake Bonneville. Lake Bonneville sediments should have been preserved if BSF evaporite deposits formed from evaporated Lake Bonneville water. BSF evaporites were deposited on pre–Lake Bonneville sediments beginning at 8.3 cal ka BP, indicating 1 to 2 m of Lake Bonneville sediments, absent at BSF but present in other parts of GSLD, were deflated between 13 cal ka BP (when Lake Bonneville desiccated) and 8.3 cal ka BP. Most deflation may have occurred under increased regional aridity from ~10 to 8 cal ka BP; during this period, highly erodible efflorescent crusts likely developed and enhanced deflation at and around BSF.

The onset of evaporite deposition, predominantly gypsum, coincides with the rise to elevated regional aridity from 8.3 to 5.4 cal ka BP. Regional aridity decreased from 5.4 to 3.5 cal ka BP, coinciding with BSF's basal halite layer deposition. Our results disprove a long-held presumption that the saline pan formed directly from the desiccation of Lake Bonneville. Instead, they show that halite-encrusted saline pan development began at BSF because the climate became less arid. The depositional record of BSF provides a lens to interpret similar saline systems. This record also suggests that dust sourced from BSF and similar saline pans and saline lakes may increase as saline systems shrink.

Acknowledgments. Funding is provided by the NSF Coupled Natural and Human Systems project award 1617473 to BBB, a Geological Society of America Graduate Student Research Grant, the Global Change and Sustainability Center at the University of Utah, the Colorado Science Society, an American Association of Petroleum Geologists Grant-in-Aid, a Continental Scientific Drilling facility graduate student travel grant, and the Utah Geological Survey. This work was made possible with the support of the U.S. Bureau of Land Management West Desert District's current and former office staff, including Kevin Oliver, Matt Preston, Mike Nelson, Cheryl Johnson, Steve Allen, Roxanne Tea, and Todd Marks. We thank Mark Shapely, Kristina Brady, and Amy Myrbo for their analytical help and discussions at the Continental Scientific Drilling facility. We thank Diego Fernandez for analyzing samples for strontium isotope ratios; Taylor Boden for sharing his GSLD gypsum dune samples with us; Scott Hynek, Quintin Sahratian, and Barbara Nash for ash preparation and analysis; Beth and Chuck Holmes for help in preliminary geochronology of sediments; Kaylee Barket Jones and Ben Marconi for vibracoring assistance; Andrea Brunelle for

https://doi.org/10.1017/qua.2023.79 Published online by Cambridge University Press

technical advice; Elliot Jagniecki and Francisca Oboh-Ikuenobe for insightful discussion; Evan Kipnis for help calibrating pXRF data; David Dinter for sedimentological discussion; Tammy Rittenour, Michelle Nelson, and Carlie Ideker for OSL dating; Peter Nielsen and Tom Dempster at Utah Core Research Center; Intrepid Potash for sampling access; and Stephanie Brock, Annie Matzke, Hannah Stintson, Lily Wetterlin, Amanda Jayo, and Melissa Wolfe for lab assistance. We appreciate our geologic mapping collaboration with Dave Miller, Tracey Felger, Vicki Langenheim, and Christian Hardwick. This article was improved by the reviews and comments of Mike Hylland, Stephanie Carnie, Lesleigh Anderson, Nicholas Lancaster, and two anonymous reviewers. The authors declare that they have no conflict of interest.

Data Availability Statement. Supplementary Data tables summarizing microprobe analytical results of volcanic ash from WS2, XRD data, pXRF measurements, unit thicknesses, smear slide data, ostracode data, regional strontium isotope samples, saline pan sand grain composition and grain size distribution data, and more detailed core stratigraphic data and correlation figures, are available at https://doi.org/10.5281/zenodo.7271700.

REFERENCES

Adams, K.D., Bills, B.G., 2016. Isostatic rebound and palinspastic restoration of the Bonneville and Provo shorelines in the Bonneville Basin, UT, NV, and ID. *Developments in Earth Surface Processes* **20**, 145–164.

Antevs, E., 1948. Climatic changes and pre-white man. *Bulletin of the University of Utah* **38**, 167–191.

Arnow, T., Stephens, D., 1990. Hydrologic Characteristics of the Great Salt Lake, Utah: 1847–1986. U.S. Geological Survey Water-Supply Paper 2332. https://doi.org/10.3133/wsp2332.

Atkinson, G.M., Finn, W.L., Charlwood, R.G., 1984. Simple computation of liquefaction probability for seismic hazard applications. *Earthquake Spectra* **1**, 107–123.

Bae, H., Park, J., Ahn, H., Khim, J.S., 2020. Shift in benthic diatom community structure and salinity thresholds in a hypersaline environment of solar saltern, Korea. *Algae* **35**, 361–373.

Balch, D.P., Cohen, A.S., Schnurrenberger, D.W., Haskell, B.J., Valero Garces, B.L., Beck, J.W., Cheng, H., Edwards, R.L., 2005. Ecosystem and paleohydrological response to Quaternary climate change in the Bonneville Basin, Utah. *Palaeogeography, Palaeoclimatology, Palaeoecology* **221**, 99–122.

Bernau, J.A., Bowen, B.B., 2021. Depositional and early diagenetic characteristics of modern saline pan deposits at the Bonneville Salt Flats, Utah, USA. *Sedimentology* **68**, 2450–2472.

Bernau, J.A., Oviatt, C.G., Clark, D.L., Bowen, B.B., 2023. Sediment Logs Compiled from the Great Salt Lake Desert, Western Utah, with a Focus on the Bonneville Salt Flats Area. Utah Geological Survey Open-File Report 754. https://doi.org/10.34191/OFR-754.

Bills, B.G., Borsa, A.A., Comstock, R.L., 2007. MISR-based passive optical bathymetry from orbit with few-cm level of accuracy on the Salar de Uyuni, Bolivia. *Remote Sensing of Environment* **107**, 240–255.

Blaauw, M., Christeny, J.A., 2011. Flexible paleoclimate age–depth models using an autoregressive gamma process. *Bayesian Analysis* **6**, 457–474.

Boden, H.T., 2016. Gypsiferous sand dune deposits on SITLA lands in the Great Salt Lake Desert project area, Tooele County, Utah. In: Comer, J.B., Inkenbrandt, P.C., Krahulec, K.A., Pinnell, M. (Eds.), *Resources and Geology of Utah's West Desert*. UGA 45. Utah Geological Association, Salt Lake City, pp. 105–130.

Bowen, B.B., Bernau, J.A., Kipnis, E.L., Lerback, J.C., Wetterlin, L., Kleba, B., 2018a. The making of a perfect racetrack at the Bonneville Salt Flats. *Sedimentary Record* **16**, 4–11.

Bowen, B.B., Kipnis, E.L., Pechmann, J.M., 2018b. Observations of salt crust thickness change at the Bonneville Salt Flats from 2003–2016. In: Emerman, S.H., Bowen, B.B., Simmons, S., and Schamel, S. (Eds.), *Geofluids of Utah*. UGA47. Utah Geological Association, Salt Lake City, pp. 247–285.

Bowen, B.B., Kipnis, E.L., Raming, L.W., 2017. Temporal dynamics of flooding, evaporation, and desiccation cycles and observations of salt crust area change at the Bonneville Salt Flats, Utah. *Geomorphology* **299**, 1–11.

Bowen, G.J., Nielson, K.E., Eglinton, T.I., 2019. Multi-substrate radiocarbon data constrain detrital and reservoir effects in Holocene sediments of the Great Salt Lake, Utah. *Radiocarbon* **61**, 905–926.

Bradbury, C.D., Jewell, P.W., Fernandez, D.P., Lerback, J.C., DeGraffenried, J.V., Petersen, E.U., 2020. Water provenance at the Old River Bed inland delta and ground water flow from the Sevier basin of central Utah during the Pleistocene–Holocene transition. *Quaternary Research* **99**, 114–127.

Bright, J., Kaufman, D.S., Oviatt, C.G., Clark, D.L., 2022. Amino Acid Racemization Geochronology Results from the Wendover Core in the Salduro Quadrangle, Utah. Utah Geological Survey Open-File Report 741. https://doi.org/10.34191/OFR-741.

Burke, R.B., Gerhard, L.C., 2000. Aragonite cementation and related sedimentary structures in Quaternary lacustrine deposits, Great Salt Lake, Utah. In: King, J.K., and Willis, G.C. (Eds.), *The Geology of Antelope Island, Davis County, Utah. Salt Lake City, Utah*. Utah Geological and Mineral Survey Miscellaneous Publication 00-1. Utah Geological and Mineral Survey, Salt Lake City, pp. 99–115.

Cahill, T.A., Gill, T.E., Reid, J.S., Gearhart, E.A., Gillette, D.A., 1996. Saltating particles, playa crusts and dust aerosols at Owens (dry) Lake, California. *Earth Surface Processes and Landforms* **21**, 621–639.

Carling, G.T., Fernandez, D.P., Rey, K.A., Hale, C.A., Goodman, M.M., Nelson, S.T., 2020. Using strontium isotopes to trace dust from a drying Great Salt Lake to adjacent urban areas and mountain snowpack. *Environmental Research Letters* **15**, 1–10.

Chen, C.Y., Maloof, A.C., 2017. Revisiting the deformed high shoreline of Lake Bonneville. *Quaternary Science Reviews* **159**, 169–189.

Clark, D.L., Oviatt, C.G., Hardwick, C., Page, D., 2020. Interim Geologic Map of the Bonneville Salt Flats and East Part of the Wendover 30′ × 60′ Quadrangles, Tooele County, Utah–year 3. Utah Geological and Mineral Survey Open-File Report 731. https://doi.org/10.34191/OFR-731.

Clavero, E., Hernández-Mariné, M., Grimalt, J.O., Garcia-Pichel, F., 2000. Salinity tolerance of diatoms from thalassic hypersaline environments. *Journal of Phycology* **36**, 1021–1034.

Cook, K.L., Halverson, M.O., Stepi, J.C., Berg, J.W., 1964. Regional gravity survey of the northern Great Salt Lake Desert and adjacent areas in Utah, Nevada, and Idaho. *Geological Society of America Bulletin* **75**, 715–740.

Cumming, B.F., Wilson, S.E., Smol, J.P., 1993. Paleolimnological potential of chrysophyte cysts and scales and of sponge spicules as indicators of lake salinity. *International Journal of Salt Lake Research* **2**, 87–92.

Cupper, M.L., 2006. Luminescence and radiocarbon chronologies of playa sedimentation in the Murray Basin, southeastern Australia. *Quaternary Science Reviews* **25**, 2594–2607.

DeDeckker, P., Forester, R.M., 1988. The use of ostracods to reconstruct continental paleoenvironmental records. In: *Ostracoda in the Earth Sciences*. Elsevier, Amsterdam, pp. 175–199.

Delorme, L.D., 1969. Ostracodes as Quaternary paleoecological indicators. *Canadian Journal of Earth Sciences* **6**, 1471–1476.

DuRoss, C.B., 2011. Liquefaction in the April 15, 2010, M 4.5 Randolph earthquake. *Utah Geological Survey: Survey Notes* 43, **1**, 7.

Dutkiewicz, A., Herczeg, A.L., Dighton, J.C., 2000. Past changes to isotopic and solute balances in a continental playa: clues from stable isotopes of lacustrine carbonates. *Chemical Geology* **165**, 309–329.

Eardley, A.J., 1938. Sediments of the Great Salt Lake, Utah. *American Association of Petroleum Geologists Bulletin* **22**, 1305–1411.

Eardley, A.J., 1962. *Gypsum Dunes and Evaporite History of the Great Salt Lake Desert*. Utah Geological and Mineral Survey Special Studies 2. Utah Geological and Mineral Survey, Salt Lake City.

Eardley, A.J., Gvosdetsky, V., Marsell, R.E., 1957. Hydrology of Lake Bonneville and sediments and soils of its basin. *Bulletin of the Geological Society of America* **88**, 1142–1201.

Egan, J., Staff, R., Blackford, J., 2015. A high-precision age estimate of the Holocene Plinian eruption of Mount Mazama, Oregon, USA. *The Holocene* **25**, 1054–1067.

Elam, W.T., Scruggs, B., Eggert, F., Nicolosi, J., 2010. Advantages and disadvantages of Bayesian methods for obtaining XRF net intensities. *Powder Diffraction* **25**, 215–215.

https://doi.org/10.1017/qua.2023.79 Published online by Cambridge University Press

Fitzgerald, V., 2019. *Chronology of Gypsum Dunes at Knolls, Utah: Refining OSL Techniques and Timing of Holocene Eolian Processes*. M.S. thesis, Department of Geology, Kansas State University, Manhattan.

Forester, R.M., 1983. Relationship of two lacustrine ostracode species to solute composition and salinity. *Geology* **11**, 435–438.

Forester, R.M., 1986. Determination of the dissolved anion composition of ancient lakes from fossil ostracodes. *Geology* **14**, 796–798.

Forester, R.M., 1987. Late Quaternary paleoclimate records from lacustrine ostracodes. In: Ruddiman, W.F., Wright, H.E.J. (Eds.), *North America and Adjacent Oceans During the Last Deglaciation*. Geological Society of America, McLean, VA, pp. 261–276.

Forester, R.M., 1988. *Nonmarine Calcareous Microfossil Sample Preparation and Data Acquisition Procedures*. U.S. Geological Survey Technical Procedure HP-78 RI, pp. 1–9.

Forester, R.M., Lowenstein, T.K., Spencer, R.J., 2005. An ostracode based paleolimnologic and paleohydrologic history of Death Valley: 200 to 0 ka. *Bulletin of the Geological Society of America* **117**, 1379–1386.

Gajardo, G.M., Beardmore, J.A., 2012. The brine shrimp Artemia: adapted to critical life conditions. *Frontiers in Physiology* **3**, 1–8.

Gilbert, G.K., 1890. Lake Bonneville. *Monographs of the U.S. Geological Survey* **1**, 438

Hajdas, I., Bonani, G., Zimmerman, S.H., Mendelson, M., Hemming, S., 2004. ^{14}C ages of ostracodes from Pleistocene lake sediments of the western Great Basin, USA—results of progressive acid leaching. *Radiocarbon* **46**, 189–200.

Hart, I., Jones, K.B., Brunelle, A., DeGraffenried, J., Oviatt, C.G., Nash, B.P., Duke, D., Young, D.C., 2022. Building a master chronology for the western Lake Bonneville Basin with stratigraphic and elemental data from multiple sites, USA. *Radiocarbon* **64**, 69–85.

Hart, W.S., Quade, J., Madsen, D.B., Kaufman, D.S., Oviatt, C.G., 2004. The ^{87}Sr/^{86}Sr ratios of lacustrine carbonates and lake-level history of the Bonneville paleolake system. *Bulletin of the Geological Society of America* **116**, 1107–1119.

Hecker, S., 1993. Quaternary tectonics of Utah with emphasis on earthquake-hazard characterization. *Utah Geological Survey*, no. **127**, 1–135.

Heilweil, V.M., Brooks, L.E., 2011. *Conceptual Model of the Great Basin Carbonate and Alluvial Aquifer System*. U.S. Geological Survey Scientific Investigations Report 2010-5193. https://doi.org/10.3133/sir20105193.

Jackson, T.R., Halford, K.J., Gardner, P.M., Garcia, A.C., 2018. Evaluating micrometeorological estimates of groundwater discharge from Great Basin desert playas. *Groundwater* **56**, 909–920.

Jacobson, G., 1988. Hydrology of Lake Amadeus, a groundwater-discharge playa in central Australia. *BMR Journal of Australian Geology and Geophysics* **10**, 301–308

Jagniecki, E.A., Rupke, A., Kirby, S., Inkenbrandt, P., 2021. *Salt Crust, Brine, and Marginal Groundwater of Great Salt Lake's North Arm (2019 to 2021)*. Utah Geological Survey Report of Investigation 283. https://doi.org/10.34191/RI-283.

Jones, D.J., 1953. Gypsum-oolite dunes, Great Salt Lake Desert, Utah. *American Association of Petroleum Geologists Bulletin* **37**, 2530–2538.

Kocurek, G., Carr, M., Ewing, R., Havholm, K.G., Nagar, Y.C., Singhvi, A.K., 2007. White Sands Dune Field, New Mexico: age, dune dynamics and recent accumulations. *Sedimentary Geology* **197**, 313–331.

Lachniet, M.S., Asmerom, Y., Polyak, V., Denniston, R., 2020. Great Basin paleoclimate and aridity linked to Arctic warming and tropical Pacific sea surface temperatures. *Paleoceanography and Paleoclimatology* **35**, 1–22.

Lanesky, D.E., Logan, B.W., Brown, R.G., Hine, A.C., 1979. A new approach to portable vibracoring underwater and on land. *Journal of Sedimentary Research* **49**, 654–657.

Lerback, J.C., Hynek, S.A., Bowen, B.B., Bradbury, C.D., Solomon, D.K., Fernandez, D.P., 2019. Springwater provenance and flowpath evaluation in Blue Lake, Bonneville basin, Utah. *Chemical Geology* **529**, 119280.

Li, Z., Demopoulos, G.P., 2005. Solubility of $CaSO_4$ phases in aqueous HCl + $CaCl_2$ solutions from 283 K to 353 K. *Journal of Chemical and Engineering Data* **50**, 1971–1982.

Lines, G.C., 1979. *Hydrology and Surface Morphology of the Bonneville Salt Flats and Pilot Valley Playa, Utah*. U.S. Geological Survey Water Supply Paper 2057. https://doi.org/10.3133/wsp2057.

Lisiecki, L.E., Raymo, M.E., 2005. A Pliocene-Pleistocene stack of 57 globally distributed benthic δ^{18}O records. *Paleoceanography* **20**, 1–17.

Louderback, L.A., Rhode, D.E., 2009. 15,000 Years of vegetation change in the Bonneville basin: the Blue Lake pollen record. *Quaternary Science Reviews* **28**, 308–326.

Lowenstein, T.K., Li, J., Brown, C.B., Roberts, S.M., Ku, T.L., Luo, S., Yang, W., 1999. 200 k.y. paleoclimate record from Death Valley salt core. *Geology* **27**, 3–6.

Mackereth, F., 1966. Some chemical observations on post-glacial lake sediments. *Philosophical Transactions of the Royal Society of London B* **250**, 12–53.

Mackey, G.N., Fernandez, D.P., 2011. High throughput Sr isotope analysis using an automated column chemistry system. In: AGU Fall Meeting Abstracts, abstract id: V31B-2525. https://ui.adsabs.harvard.edu/abs/2011AGUFM.V31B2525M/abstract.

Madsen, D.B., Rhode, D.E., 1990. Early Holocene pinyon (*Pinus monophylla*) in the northeastern Great Basin. *Quaternary Research* **33**, 94–101.

Madsen, D.B., Schmitt, D.N., Page, D.J., 2015. *The Paleoarchaic Occupation of the Old River Bed Delta*. University of Utah Press, Salt Lake City.

Mason, J.L., Kipp, K.L., 1998. Hydrology of the Bonneville Salt Flats, Northwestern Utah, and Simulation of Ground-Water Flow and Solute Transport in the Shallow-Brine Aquifer. U.S. Geological Survey Professional Paper 1585. https://doi.org/10.3133/pp1585.

Menking, K.M., Anderson, R.Y., 2003. Contributions of La Niña and El Niño to middle Holocene drought and late Holocene moisture in the American Southwest. *Geology* **31**, 937–940.

Mensing, S.A., Sharpe, S.E., Tunno, I., Sada, D.W., Thomas, J.M., Starratt, S., Smith, J., 2013. The Late Holocene Dry Period: multiproxy evidence for an extended drought between 2800 and 1850 cal yr BP across the central Great Basin, USA. *Quaternary Science Reviews* **78**, 266–282.

Miller, D.M., Felger, T.J, and Langenheim V.E., 2021. Geologic and Geophysical Maps of the Newfoundland Mountains and Part of the Adjacent Wells 30′ x 60′ Quadrangles, Box Elder County, Utah. Utah Geological Survey Miscellaneous Publication 173DM. https://doi.org/10.34191/MP-173DM.

Morad, S., 1998. Carbonate cementation in sandstones: controls on distribution patterns and geochemical evolution. In: *Carbonate Cementation in Sandstones: Distribution Patterns and Geochemical Evolution*. Blackwell Science, Oxford. pp. 1–27.

Morrison, R., 1966. Predecessors of Great Salt Lake. *Guidebook to the Geology of Utah 20*. Utah Geological Association, Salt Lake City, pp. 77–104.

Moutoux, T.E., 1995. Palynological and Tephra Correlations among Deep Wells in the Modern Great Salt Lake, Utah, USA: Implications for a Neogene through Pleistocene Climatic Reconstruction. M.S. thesis, University of Arizona, Tuscon.

Munroe, J.S., Norris, E.D., Carling, G.T., Beard, B.L., Satkoski, A.M., Liu, L., 2019. Isotope fingerprinting reveals western North American sources of modern dust in the Uinta Mountains, Utah, USA. *Aeolian Research* **38**, 39–47.

Nash, B.P., 1992. Analysis of oxygen with the electron microprobe: applications to hydrated glass and minerals. *American Mineralogist* **77**, 453–457.

National Academies of Sciences, Engineering and Medicine, 2020. Effectiveness and Impacts of Dust Control Measures for Owens Lake. https://doi.org/10.17226/25658.

Nolan, T.B., 1927. Potash brines in the Great Salt Lake Desert, Utah. In: *Contributions to Economic Geology*. Part I, *Metals and Nonmetals Except Fuels*. Bulletin No. 795-B U.S. Government Printing Office, Washington, DC, pp. 25–44. https://doi.org/10.3133/b795B.

Oviatt, C.G., 2014. *The Gilbert Episode in the Great Salt Lake Basin, Utah*. Utah Geological Miscellaneous Publication 14-3.

Oviatt, C.G., 2015. Chronology of Lake Bonneville, 30,000 to 10,000 yr BP. *Quaternary Science Reviews* **110**, 166–171.

Oviatt, C.G., 2017. Ostracodes in Pleistocene Lake Bonneville, eastern Great Basin, North America. *Hydrobiologia* **786**, 125–135.

Oviatt, C.G., 2021. Geomorphic controls on sedimentation in Pleistocene Lake Bonneville, eastern Great Basin. In Starratt, S.W., Rosen, M.R. (Eds.), *From Saline to Freshwater–The Diversity of Western Lakes in Space and Time. Geological Society of America Special Paper* **536**, 53–66.

https://doi.org/10.1017/qua.2023.79 Published online by Cambridge University Press

Oviatt, C.G., Atwood, G., Thompson, R.S., 2021. History of Great Salt Lake, Utah, USA: since the termination of Lake Bonneville. In: Rosen, R.M. (Ed.), *Limnogeology: Progress, Challenges and Opportunities*. Springer Nature, Cham, Switzerland, pp. 233–271.

Oviatt, C.G., Clark, D.L., Bernau, J.A., Bowen, B.B., 2020. Data on the Surficial Deposits of the Great Salt Lake Desert, Bonneville Salt Flats and East Part of the Wendover 30′ x 60′ Quadrangles, Tooele County, Utah. Utah Geological Survey Open-File Report 724. https://doi.org/10.34191/OFR-724.

Oviatt, C.G., Habiger, G.D., Hay, J.E., 1994. Variation in the composition of Lake Bonneville marl—a potential key to lake-level fluctuations and paleoclimate. *Journal of Paleolimnology* 11, **1**, 19–30.

Oviatt, C.G., Madsen, D.B., Miller, D.M., Thompson, R.S., McGeehin, J.P., 2015. Early Holocene Great Salt Lake, USA. *Quaternary Research* **84**, 57–68.

Oviatt, C.G., Madsen, D.B., Schmitt, D.N., 2003. Late Pleistocene and early Holocene rivers and wetlands in the Bonneville basin of western North America. *Quaternary Research* **60**, 200–210.

Oviatt, C.G., Pigati, J.S., Madsen, D.B., Rhode, D.E., Bright, J., 2018. *Juke Box Trench—A Valuable Archive of Late Pleistocene and Holocene Stratigraphy in the Bonneville Basin, Utah*. Utah Geological Survey Miscellaneous Publication 18-1. Utah Geological and Mineral Survey, Salt Lake City.

Oviatt, C.G., Shroder, J.F., 2016. *Lake Bonneville: A Scientific Update*. Developments in Earth Surface Processes. Elsevier, Amsterdam.

Palacios-Fest, M.R., Duke, D., Young, D.C., Kirk, J.D., Oviatt, C.G., 2021. A paleo-lake and wetland paleoecology associated with human use of the distal Old River Bed Delta at the Pleistocene–Holocene transition in the Bonneville Basin, Utah, USA. *Quaternary Research* **106**, 1–19.

Paradis, O.P., 2019. *Great Salt Lake Ooids: Insights into rate of Formation, Potential as Paleoenvironmental Archives, and Biogenicity*. Ph.D. dissertation, University of Southern California, Los Angeles.

Pedone, V.A., Oviatt, C.G., 2013. South to north flow in Lake Bonneville: evidence from carbonate mineralogy and geochemistry. *Geological Society of America Abstract Programs*. 7123 p.

Potapova, M., 2011. Patterns of diatom distribution in relation to salinity. In: Seckbach, J., Kociolek, P. (Eds.), *The Diatom World*. Cellular Origin, Life in Extreme Habitats and Astrobiology 19. Springer, Dordrecht, pp. 313–332.

Radwin, M.H., Bowen, B.B., 2021. Mapping mineralogy in evaporite basins through time using multispectral Landsat data: examples from the Bonneville basin, Utah, USA. *Earth Surface Processes and Landforms* **46**, 1160–1176.

R Core Team, 2018. *R: A Language and Environment for Statistical Computing*. R Foundation for Statistical Computing, Vienna, Austria. https://www.R-project.org.

Reed, J.A., 2007. *The Paleontological Stratigraphic Interval Construction and Analysis Tool*. M.S. thesis, Iowa State University, Ames.

Reimer, P.J., Austin, W.E.N., Bard, E., Bayliss, A., Blackwell, P.G., Bronk Ramsey, C., Butzin, M., *et al.*, 2020. The IntCal20 Northern Hemisphere Radiocarbon Age Calibration Curve (0-55 cal kBP). *Radiocarbon* **62**, 725–757.

Rey, K.A., Mayo, A.L., Tingey, D.G., Nelson, S.T., 2016. Late Pleistocene to early Holocene sedimentary history of the Lake Bonneville Pilot Valley embayment, Utah-Nevada, USA. In: Oviatt, C.G., Shroder, J.F. (Eds.), *Lake Bonneville: A Scientific Update*. Developments in Earth Surface Processes 20. Elsevier, Amsterdam, pp. 184–220.

Reynolds, R.L., Yount, J.C., Reheis, M., Goldstein, H.L., Chavez, P., Fulton, R.S., Whitney, J., Fuller, C.C., Forester, R.M., 2007. Dust emission from wet and dry playas in the Mojave Desert, USA. *Earth Surface Processes and Landforms* **34**, 613–628.

Rhode, D.E., 2016. Quaternary vegetation changes in the Bonneville Basin. In: Oviatt, C.G., Shroder, J.F. (Eds.), *Lake Bonneville: A Scientific Update*. Developments in Earth Surface Processes 20. Elsevier, Amsterdam, pp. 420–441.

Rodríguez-Pascua, M.A., Calvo, J.P., De Vicente, G., Gómez-Gras, D., 2000. Soft-sediment deformation structures interpreted as seismites in lacustrine sediments of the Prebetic Zone, SE Spain, and their potential use as indicators of earthquake magnitudes during the Late Miocene. *Sedimentary Geology* **135**, 117–135.

Rosen, M.R., 1994. The importance of groundwater in playas: a review of playa classifications and the sedimentology and hydrology of playas. *Geological Society of America Special Papers* **289**, 1–18.

Rothwell, R.G., Croudace, I.W., 2015. Twenty years of XRF core scanning marine sediments: What do geochemical proxies tell us? In: Croudace, I., Rothwell, R. (Eds.), *Micro-XRF Studies of Sediment Cores: Developments in Paleoenvironmental Research*, Vol 17. Springer, Dordrecht, pp. 25–102.

Smith, R.P., Breckenridge, R.P., Wood, T.R., 2012, *Assessment of Geothermal Resource Potential at a High-Priority Area on the Utah Testing and Training Range-South (UTTR-S)*. Idaho National Laboratory, Idaho Falls. https://inldigitallibrary.inl.gov/sites/sti/sti/5411185.pdf.

So, R.T., Lowenstein, T.K., Jagniecki, E., Tierney, J.E., Feakins, S.J., 2023. Holocene water balance variations in Great Salt Lake, Utah: application of GDGT indices and the ACE salinity proxy. *Paleoceanography and Paleoclimatology* **38**, e2022PA004558.

Steponaitis, E., Andrews, A., McGee, D., Quade, J., Hsieh, Y.T., Broecker, W.S., Shuman, B.N., Burns, S.J., Cheng, H., 2015. Mid-Holocene drying of the U.S. Great Basin recorded in Nevada speleothems. *Quaternary Science Reviews* **127**, 174–185.

Thompson, R.S., Oviatt, C.G., Honke, J.S., McGeehin, J.P., 2016. Late Quaternary changes in lakes, vegetation, and climate in the Bonneville Basin reconstructed from sediment cores from Great Salt Lake. In: Oviatt, C.G., Shroder, J.F. (eds.), *Lake Bonneville: A Scientific Update*. Developments in Earth Surface Processes 20. Elsevier, Amsterdam, pp. pp. 184–220.

Thompson, R.S., Toolin, L.J., Forester, R.M., Spencer, R.J., 1990. Accelerator-mass spectrometer (AMS) radiocarbon dating of Pleistocene lake sediments in the Great Basin. *Palaeogeography, Palaeoclimatology, Palaeoecology* **78**, 301–313.

Turk, L.J., 1973. *Hydrogeology of the Bonneville Salt Flats, Utah*. Utah Geological and Mineral Survey Water Resources Bulletin 19. Utah Geological and Mineral Survey, Salt Lake City, pp. 1–82.

Turk, L.J., Davis, S.N., Bingham, C.P., 1973. Hydrogeology of lacustrine sediments, Bonneville Salt Flats, Utah. *Economic Geology* **68**, 65–78.

Ulmer-Scholle, D.S., Scholle, P.A., Schieber, J., Raine, R.J., 2014. Diagenesis: carbonate cements and authigenic precipitates. In: *A Color Guide to the Petrography of Sandstones, Siltstones, Shales and Associated Rocks*. AAPG Memoir 109. American Association of Petroleum Geologists, Tulsa, OK, pp. 310–334.

Vanhaecke, P., Siddall, S.E., Sorgeloos, P., 1984. International study on *Artemia*. XXXII: combined effects of temperature and salinity on the survival of *Artemia* of various geographical origins. *Journal of Experimental Marine Biology and Ecology* **80**, 259–275.

Williams, S.K., 1994. Late Cenozoic tephrostratigraphy of deep sediment cores from the Bonneville Basin, northwest Utah. *Geological Society of America Bulletin* **106**, 1517–1530.

Wurtsbaugh, W.A., Miller, C., Null, S.E., Justin De Rose, R., Wilcock, P., Hahnenberger, M., Howe, F., *et al.*, 2017. Decline of the world's saline lakes. *Nature Geoscience* **10**, 816–823.

Xingqi, L., Dong, H., Rech, J.A., Matsumoto, R., Bo, Y., Yongbo, W., 2008. Evolution of Chaka Salt Lake in NW China in response to climatic change during the Latest Pleistocene–Holocene. *Quaternary Science Reviews* **27**, 867–879.

Yucel, M., Klatt, J.M., Benzerara, K., Boyd, E.S., Dunham, E.C., Fones, E.M., Fang, Y., *et al.*, 2020. An ecological perspective on dolomite formation in Great Salt Lake, Utah. *Frontiers in Earth Science* **8**, 24.

Zhang, M., Liu, X., 2020. Climate changes in the Qaidam Basin in NW China over the past 40 kyr. *Palaeogeography, Palaeoclimatology, Palaeoecology* **551**, 109679.

Zimmerman, S.R.H., Steponaitis, E., Hemming, S.R., Zermeño, P., 2012. Potential for accurate and precise radiocarbon ages in deglacial-age lacustrine carbonates. *Quaternary Geochronology* **13**, 81–91.

APPENDIX A: OSL DATA

OSL dating yielded post-Bonneville ages for samples from pre-Bonneville sediments. Dated sediments were very fine-grained and primarily consisted of endogenic carbonates, leaving processed OSL samples with very little material

https://doi.org/10.1017/qua.2023.79 Published online by Cambridge University Press

https://doi.org/10.1017/qua.2023.79 Published online by Cambridge University Press

Table A1. Optically stimulated luminescence (OSL) dating data.[a]

Core	Depth (cm)	No. of aliquots	Dose rate (Gy/ka)	Equivalent dose ± 2σ (Gy)	OSL age (ka)	Age error (1σ) (ka)	In situ H_2O (%)	Dose rate samples	KK (%) (±0.4)	Rb (ppm) (±2.6)	Th (ppm) (±0.5)	U (ppm) (±0.3)	Cosmic (Gy/ka)
SOL	40-55[b]	8 (29)	2.06 ± 0.08	39.61 ± 2.87	9.24	1.71	29.9	U, M, L	1.19	57.2	4.1	3.9	0.25 ± 0.03
SOL	92-307	8 (25)	1.77 ± 0.07	19.81 ± 4.61	1.2	1.59	34.8	U, M, L	1.04	5.3	3.4	3.9	0.18 ± 0.02
WS2	105-120	18 (20)	2.49 ± 0.10	14.69 ± 3.47	5.91	0.88	14	U (25%)	1.32	57.0	4.6	3.2	0.21 ± 0.02
								M (50%)	1.45	63.4	5.3	3.4	
								L (25%)	1.41	64.7	5.0	3.4	
WS2	266-281	17 (32)	2.27 ± 0.09	29.47 ± 3.79	13	1.34	22.5	U (25%)	0.99	35.2	3.1	4.2	0.17 ± 0.02
								M (50%)	1.43	62.2	5.3	3.5	
								L (25%)	1.57	72.7	6.0	3.1	
SC1	70-85	21 (36)	1.91 ± 0.08	14.89 ± 3.01	7.78	1.11	9.5	U (25%)	0.93	43.3	3.4	4.0	0.24 ± 0.02
								M (50%)	0.99	43.5	3.5	3.2	
								L (25%)	0.78	33.8	2.7	4.4	
SC1	315-330	17 (18)	2.28 ± 0.09	31.73 ± 4.20	3.9	1.45	7.3	U (25%)	1.43	62.2	5.4	4	0.18 ± 0.02
								M (50%)	1.25	54.9	4.5	4	
								L (25%)	0.8	29.5	2.5	4.2	

[a]K, Rb, Th, and U measured from "Dose rate samples" used for environmental dose rate; dose rate data from above (U), below (L), and within (M) sampled interval are noted. Data are from the Utah State University Luminescence Lab. SOL samples were measured in 2018. WS2 and SC1 samples were measured in 2020. Based on acid treatment and density separation, OSL measurement materials are considered to be quartz and possibly feldspar. However, no scanning electron microscopy measurements were made to confirm mineralogy.
[b]Sample from an injectite. Age reversal is interpreted as a result of vertical sediment movement.

and very fine grain size (which are challenging samples to measure with OSL). OSL ages were strongly influenced by the environmental dose rate, which changed if Lake Bonneville sediment (and water) were assumed to have covered sample locations. There is overwhelming stratigraphic evidence that Lake Bonneville sediments were eroded locally. Past deflation and potentially the enrichment of potash-rich brine (which could influence the environmental dose rate) are also complicating factors in interpreting OSL material here (Table A1).

APPENDIX B: VOLCANIC ASH DATA

A 1-mm-thick volcanic ash layer was encountered at a depth of 204.5 cm in the WS2 core. Volcanic glass shards were identified in smear slides. The volcanic ash was chemically characterized with microprobe analysis by B. Nash (Department of Geology and Geophysics at the University of Utah) with a Cameca SX-50 microprobe. Microprobe analytical conditions are described by Nash (1992). Sediment was treated with nitric acid to remove carbonates and hydrofluoric acid to remove further impurities. Microprobe elemental composition was compared to the Mazama ash from the nearby Jukebox trench (Oviatt et al., 2018) and a laboratory standard (Mineral Mountain obsidian; Nash, 1992). Elemental information is available here: https://doi.org/10.5281/zenodo.7271700.

Microprobe analysis indicates that the WS2 204.5 cm ash is silicic and does not match any other ash layer in this region (it does not match the Mazama ash or any of the >2900 ash samples measured by the Nash laboratory; Nash, B., personal communication, 2019). It resembles but is not unequivocally identical to, ash dating to ∼1.24 Ma from a core from the northern portion of GSL (brg-1740; Moutoux, 1995). We interpret different sources and timing for the WS2 204.5 cm and brg-1740 ashes, because ashes dating from <0.2 to >1.1 Ma were identified in the 171-m-deep Wendover core, collected south of BSF (Williams, 1994). Furthermore, the WS2 age–depth model indicates this ash was deposited at ∼35 cal ka BP. Finally, it is unlikely that the WS2 204.5 cm ash horizon is reworked brg-1740, because the horizon is well defined and not distributed, as would be expected if it was a reworked deposit.

APPENDIX C: SOFT-SEDIMENT DEFORMATION FEATURES

At least three depth intervals with soft-sediment deformation features exist across the cores. Soft-sediment deformation features include centimeter-scale normal faults, fault sets, and vertically to sub-vertically oriented injectites (injectites only occur at SOL). Some faults and injectites extend vertically for tens of centimeters. Similar faults and injectites exist in other GSLD shallow cores and ditch exposures surrounding BSF, indicating that the soft-sediment deformation features are not coring artifacts. We describe deformation features from oldest to youngest.

There are small, poorly defined, soft-sediment deformation features in the upper portion of unit VII in SC1 (small faults) and SOL (a sub-vertical injectite; Fig. 4). Unit VI has a tens-of-centimeters-long fault in SC1 and a fault set in SOL. Immediately below the top of unit IV, there are several normal faulting features in WS2, SC1, and SOL; SOL also has an injectite in unit IV. The uppermost soft-sediment deformation feature occurred in the mid-upper part of unit III, with the strongest deformation features existing in western sediments at SOL (faulting and an injectite); some faulting is seen in WS2, and subtle faulting exists in unit III at SC1. This pattern suggests that if this feature is due to seismicity, a fault west of BSF contributed to deformation, or shallower near-lakeshore sediments were more susceptible to deformation. If injectites are formed by seismicity, there must have been at least M_L (local magnitude) 4.5–5.0 seismicity to support liquefaction and sand mobilization (Atkinson et al., 1984; Rodríguez-Pascua et al., 2000; DuRoss, 2011).

If the uppermost extent of each soft-sediment deformation feature roughly aligns with its onset, then deformation features formed at approximately 41, 36, and 30 cal ka BP. Alternatively, if the soft-sediment deformation features did not originate from seismicity, they may be from desiccation associated with deflationary events; sediment loading has also been proposed as a mechanism for their formation.

Limited information exists regarding Pleistocene–Holocene faulting activity in the Wendover graben. Previous research suggested that vertical displacement from Holocene faulting might have contributed to the westward tilt of BSF evaporites (Bowen et al., 2018a). However, this tilting appears evident primarily in the uppermost bedded halite layers and not in deeper ones. This raises questions about whether the tilting is tectonic or hydrodynamic, as similar basin-edge decreases in saline pan elevation have been observed in other basins (Bills et al., 2007).

A preliminary report identified a suspect Holocene fault with 0.6 m of displacement in presumed Lake Bonneville deposits near a Holocene spring along the eastern Silver Island Mountains to the west of BSF, suggesting recent faulting in this area (Hecker, 1993; Madsen, D., personal communication, 2022). Only post-Bonneville and pre-Bonneville sediments (Lake Bonneville sediments were absent) were identified during a more recent examination of sediments collected near the suspected Holocene fault (Bernau et al., 2023).

APPENDIX D: RELATIVE ELEMENTAL OCCURRENCES

pXRF geochemical measurements exhibit significant variability across cores. Key elemental trends are highlighted in Figure 5 in the main text. Oolitic sand beds have distinctive features, including low Fe/Mn, Si/Al, and Fe/Al ratios; decreases in Al, Ti, Fe, and Si counts; and high Cl/Ca, Sr/Ca, and S/Al ratios. Bedded evaporites display high Sr/Ca and S/Ca ratios, indicating gypsum presence. Mg/Ca and Fe/Mn ratios, along with counts for Ca, Mg, and Mn, reflect relative carbonate changes and water chemistry over time. High Mg/Ca ratios reflect intervals with more XRD-measured dolomite and calcite (with some high-Mg calcite). The Fe/Mn ratio, commonly used for interpreting redox states or catchment changes (Mackereth, 1966), proves valuable for stratigraphic correlation. Higher Fe/Mn ratios correspond to periods with fewer endogenic carbonates, while lower Fe/Mn ratios correspond to dry periods and occur below several oolitic sand beds.

https://doi.org/10.1017/qua.2023.79 Published online by Cambridge University Press